

The Science Cases for Building a Band 1 Receiver Suite for ALMA

J. Di Francesco^{1,2}, D. Johnstone^{1,2}, B. Matthews^{1,2}, N. Bartel³, L. Bronfman⁴,
S. Casassus⁴, S. Chitsazzadeh^{2,5}, M. Cunningham⁶, G. Duchêne^{7,8}, J. Geisbuesch⁹,
A. Hales¹⁰, P.T.P. Ho¹¹, M. Houde⁵, D. Iono¹², F. Kemper¹¹, A. Kepley¹⁰, P.M. Koch¹¹,
K. Kohno¹³, R. Kothes⁹, S-P. Lai¹⁴, K.Y. Lin¹¹, S.-Y. Liu¹¹, B. Mason¹⁰, T.J. Maccarone¹⁵,
N. Mizuno¹², O. Morata¹¹, G. Schieven¹, A.M.M. Scaife¹⁶, D. Scott¹⁷, H. Shang¹¹,
M. Shimojo¹², S. Takakuwa¹¹, J. Wagg^{18,19}, A. Wootten¹⁰, F. Yusef-Zadeh²⁰

¹National Research Council Canada, 5071 West Saanich Rd, Victoria, BC, V9E 2E7, Canada

²Dept. of Physics & Astronomy, University of Victoria, Victoria, BC, V8P 1A1, Canada

³Dept. of Physics and Astronomy, York University, Toronto, M3J 1P3, ON, Canada

⁴Dept. de Astronomía, Universidad de Chile, Casilla 36-D, Santiago, Chile

⁵Dept. of Physics and Astronomy, The University of Western Ontario, London, ON, N6A 3K7, Canada

⁶School of Physics, University of New South Wales, Sydney, NSW 20152, Australia

⁷Astronomy Dept., University of California, Berkeley, CA 94720-3411, USA

⁸Université Joseph Fourier - Grenoble 1/CNRS, LAOG UMR 5571, BP 53, 38041 Grenoble, France

⁹National Research Council Canada, P.O. Box 248, Penticton, BC, V2A 6J9, Canada

¹⁰National Radio Astronomy Observatory, 520 Edgemont Road, Charlottesville, Virginia 22903, USA

¹¹Academia Sinica, Institute of Astronomy and Astrophysics, P.O. Box 23-141, Taipei 10617, Taiwan

¹²National Astronomical Observatory of Japan, 2-21-1 Osawa, Mitaka, Tokyo, 181-8588, Japan

¹³Institute of Astronomy, The University of Tokyo, 2-21-1 Osawa, Mitaka, Tokyo 181-0015, Japan

¹⁴Institute of Astronomy and Dept. of Physics, National Tsing Hua University, Taiwan

¹⁵Department of Physics, Texas Tech University, Lubbock, TX, 79409-1051, USA

¹⁶School of Physics and Astronomy, University of Southampton, Southampton, Hampshire, S017 1BJ, UK

¹⁷Dept. of Physics and Astronomy, University of British Columbia, Vancouver, BC, V6T 1Z1, Canada

¹⁸European Southern Observatory, Alonso de Cordova 3107, Vitacura, Casilla 19001, Santiago 19, Chile

¹⁹Astrophysics Group, Cavendish Laboratory, JJ Thomson Avenue, Cambridge, CB30HE, UK

²⁰Dept. of Physics and Astronomy and Center for Interdisciplinary Research in Astronomy, Northwestern University, Evanston, IL 60208, USA

1. Executive Summary

The ALMA Band 1 project aims to provide a low-cost solution to one of the original design goals of the Atacama Large Millimeter/submillimeter Array (ALMA), access to frequencies of ~ 40 GHz at high resolution and sensitivity from the southern hemisphere. In this document, we present a set of compelling science cases for construction of the ALMA Band 1 receiver suite. For these, we assume in tandem the updated nominal Band 1 frequency range of 35-50 GHz and its likely extension up to 52 GHz that together optimize the Band 1 science return.

A comprehensive comparison of ALMA and the Jansky VLA (JVLA) over 40-50 GHz finds ALMA having similar sensitivity at lower frequencies but the edge in sensitivity (e.g., up to a factor of ~ 2) at higher frequencies. In addition, ALMA's larger primary beams allow this sensitivity to be obtained over wider fields. Furthermore, ALMA Band 1 images will have significantly greater fidelity than those from the JVLA since ALMA has a larger number of instantaneous baselines. ALMA's smaller dishes (and the ACA, if needed) in principle can allow the recovery of more extended emission. Finally, ALMA Band 1 will likely include frequencies of 50-52 GHz that the JVLA simply cannot observe.

The scope of the science cases ranges from nearby stars to the re-ionization edge of the Universe. Two cases provide additional leverage on the present ALMA Level One Science Goals and are seen as particularly powerful motivations for building the Band 1 receiver suite: (1) detailing the evolution of grains in protoplanetary disks, as a complement to the gas kinematics, requires continuum observations out to 35 GHz (~ 9 mm); and (2) detecting CO 3-2 line emission from galaxies like the Milky Way during the epoch of re-ionization, i.e., $6 < z < 10$, also requires Band 1 receiver coverage. Indeed, Band 1 will increase the volume of the observable Universe in CO lines by a factor of 8. The range of Band 1 science is very broad, however, and also includes studies of galaxy clusters (i.e., via the Sunyaev-Zel'dovich Effect), very small dust grains in the ISM, the Galactic Center, solar studies, pulsar wind nebulae, radio supernovae, X-ray binaries, dense cloud cores, complex carbon-chain molecules, ionized gas (e.g., in HII regions), masers, magnetic fields in the dense ISM, jets and outflows from young stars, the co-evolution of star formation with active galactic nuclei, and the molecular mass in moderate redshift galaxies.

2. Introduction

The Atacama Large Millimeter/submillimeter Array (ALMA) will be a single research instrument composed of at least fifty 12-m antennas in its 12-m Array and twelve 7-m high-precision antennas plus four 12-m antennas in its compact array (the Atacama Compact Array; ACA), located at a very high altitude of 5000 m on the Chajnantor plateau of the Chilean Andes. The weather conditions at the ALMA site will allow transformational research into the physics of the cold Universe across a wide range of wavelengths, from radio to submillimeter. Thus, ALMA will be capable of probing the first stars and galaxies and directly imaging the disks in which planets are formed. ALMA will be the pre-eminent astronomical imaging and spectroscopic instrument at millimetre/submillimetre wavelengths for decades to come. It will provide scientists with capabilities and wavelength coverage that complement those of other key research facilities of its era, such as the James Webb Space Telescope (JWST), 30-m class Giant Segmented Mirror Telescopes (GSMTs), and the Square Kilometer Array (SKA).

ALMA will revolutionize many areas of astronomy and an amazing breadth of science has already been proposed (see, for example, the ALMA Design Reference Science Plan). The technical requirements of the ALMA Project are, however, driven by three specific Level One Science Goals:

- (1) The ability to detect spectral line emission from CO or CII in a normal galaxy like the Milky Way at a redshift of $z = 3$, in less than 24 hours of observation.
- (2) The ability to image the gas kinematics in a solar-mass protostellar/protoplanetary disk at a distance of 150 pc (roughly the distance of the star-forming clouds in Ophiuchus or Corona Australis), enabling one to study the physical, chemical, and magnetic field structure of the disk and to detect the tidal gaps created by planets undergoing formation.
- (3) The ability to provide precise images at an angular resolution of $0.1''$. Here the term “precise image” means an accurate representation of the sky brightness at all points where the brightness is greater than 0.1% of the peak image brightness. This requirement applies to all sources visible to ALMA that transit at an elevation greater than 20° .

ALMA was originally envisioned to provide access to all frequencies between 31 GHz and 950 GHz accessible from the ground. During a re-baselining exercise undertaken in 2001, the entire project was scrutinized to find necessary cost savings. The two lowest receiver frequencies, Bands 1 and 2, covering 31–45 GHz and 67–90 GHz respectively, were among those items delayed beyond the start of science operations. Nevertheless, Band 1 was re-affirmed as a high priority future item for ALMA.

In May 2001, John Richer and Geoff Blake prepared the document *Science with Band*

1 (31–45 GHz) on ALMA as part of the re-baselining exercise. Key arguments for Band 1 receivers included their abilities to: (1) enable exciting science opportunities, bringing in a wider community of users; (2) be a significantly faster imaging and survey instrument than the upgraded VLA (now known as the Jansky VLA or JVLA), especially due to the larger primary beam; (3) provide access to the southern sky at these wavelengths; (4) allow excellent science possible even in “poor” weather; (5) be a relatively cheap and reliable receiver to build and maintain; and (6) be a very useful engineering/debugging tool for the entire array given the lower contribution of the atmosphere at many of its frequencies relative to other bands.

The Richer/Blake document was followed by an ASAC Committee Report in October 2001, after the addition of Japan into the ALMA project re-opened the question of observing frequency priorities for those Bands which had been put on hold during re-baselining. The unanimous recommendation of the ASAC was to put Band 10 as top priority, followed by a very high priority Band 1. At that time, the key science cases for Band 1 receivers were seen to be (1) high-resolution Sunyaev-Zel’dovich effect (SZE) imaging of cluster gas at all redshifts; and (2) mapping the cold ISM in Galaxies at intermediate and high redshift.

The scientific landscape has changed significantly since 2001 and thus it is time to re-examine the main science drivers for ALMA Band 1 receivers, even reconsidering the nominal frequency range of Band 1 itself to optimize the science return. In addition, the ALMA Development process has begun, and now is the time to put forth the best case for longer wavelength observing with ALMA. In October 2008, two dozen astronomers from around the globe met in Victoria, Canada to discuss Band 1 science. This paper summarizes the outstanding cases made possible with Band 1 that were highlighted at that meeting and since. In Section 3, we describe the new nominal Band 1 frequency range of 35-50 GHz, and its likely extension to 52 GHz. In Section 4, we present two science cases that reaffirm and enhance the already established ALMA Project Level One Science Goals. Section 5 discusses both weather considerations at the ALMA site and compares the observing capabilities of ALMA and the JVLA over Band 1 frequencies. In Section 6, we provide a selection of continuum and line science cases that reinforce the breadth and versatility of the Band 1 receiver suite. Finally, Section 7 briefly summarizes the report.

3. The Band 1 Frequency Range

Band 1 was originally defined as 31.3–45 GHz, with the lower end set to the lower edge of a frequency range assigned to radio astronomy and the upper set to include SiO $J=1-0$ emission at 43 GHz. Receiver technology advances, however, have made it possible to widen and shift the Band 1 range and optimize the science return of Band 1. For example, a wider range and shift to higher frequencies will allow molecular emission from galaxies at a wider range of (slightly lower) redshifts to be explored. Also, it will allow molecular emission from several new species in our Galaxy to be probed. (Of course, this shift does in turn remove the ability to detect molecular emission from some higher redshift galaxies and some other Galactic transitions.) Furthermore, a shift to higher frequencies for Band 1 will improve (slightly) the angular resolution of continuum observations and better exploit the advantages of the dry ALMA site.

A review of the nominal frequency range by the Band 1 Science Team (i.e., several authors of this document) in June 2012 resulted in a proposed new Band 1 frequency range definition, nominally 35–50 GHz with a likely extension up to 52 GHz. The shift up to 50 GHz will allow the important line CS $J=1-0$ at 48.99 GHz to be observable with ALMA. In addition, the nominal range of 35–50 GHz alone is itself $\sim 10\%$ wider than before. As it will provide the highest sensitivities, the nominal range will be preferred for high-redshift science. The extension to 50–52 GHz, which the JVLA cannot observe, may be somewhat adversely affected by atmospheric O₂, resulting in lower relative sensitivity. Since numerous transitions of other interesting molecules have rest frequencies at 50–52 GHz, however, this extension will allow such emission to be probed toward sources in our Galaxy. This document has been updated in September 2012 to reflect the new nominal frequency range and the extension. See Section 5 for a comparison of the sensitivities and imaging characteristics of ALMA and the JVLA over Band 1 frequencies.

4. Level One Science Cases for Band 1

In this section, we present two science cases that reaffirm and enhance the already established ALMA Project Level One Science Goals: Evolution of Grains in Disks Around Stars (§4.1) and The First Generation of Galaxies (§4.2). Further science cases are presented in §6.

4.1. Evolution of Grains in Disks Around Stars

4.1.1. *Protoplanetary Disks*

Planet formation takes place in disks of dust and gas surrounding young stars. It is within these gas-rich protoplanetary disks that dust grains must agglomerate from the sub-micron sizes associated with the interstellar medium to larger pebbles, rocks and planetesimals, if planets are ultimately to be formed. The timescale of this agglomeration process is thought to be a few tens of Myr for terrestrial planets, while the process leading to the formation of giant planet cores remains uncertain. Core accretion models require at least a few Myr to form Jovian planets (Pollack et al. 1996), while dynamical instability models could form giant planets on orbital timescales ($t \ll 1$ Myr; Boss 2005).

Gravitational instability models require high disk masses to form planets. So far, most accurate disk mass estimates come from submillimeter and millimeter observations, where the dust is optically thin. Andrews & Williams (2007a, 2007b) show that submillimeter observations of dozens of protoplanetary disks reveal that only one system could be gravitationally unstable, conflicting with the high frequency of Jovian planets seen around low mass stars. Have these relatively young (1–6 Myr) systems already formed planets, or is most of the dust mass locked into larger grains and therefore not accounted for in submillimeter and millimeter observations? If grain growth to centimeter sizes has occurred, most of a disk’s dust mass would reside in the large particle population, which would emit at longer millimeter and centimeter wavelengths. Figure 1 from Greaves et al. (in prep.) compares disk masses for objects in Taurus and Ophiuchus derived from 9 mm and 1.3 mm dust fluxes. The longer wavelength masses are found to be generally higher than the shorter wavelength values, indicating that a significant fraction of the disks’ total dust masses are indeed locked up in larger grains.

Identifying *where* and *when* dust coagulation occurs is critical to constrain current models of planetary formation. Growth from sub-micron to micron-sized particles can be traced with infrared spectroscopy and imaging polarimetry. The next step, growth beyond micron

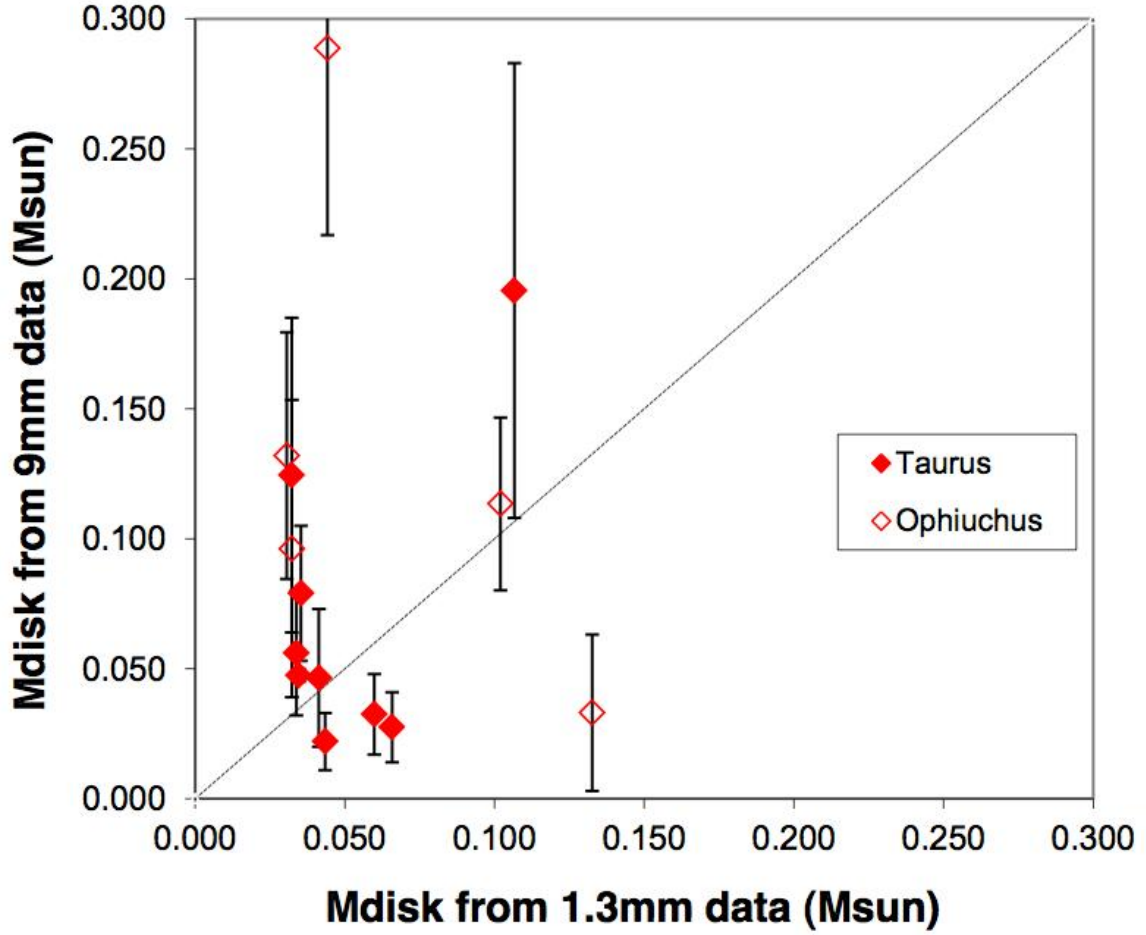


Fig. 1.— Disk masses measured from 9 mm continuum emission compared to those measured from 1.3 mm continuum emission in the regions of Taurus and Ophiuchus. Many disks show higher mass measurements at the longer wavelength, indicating the presence of larger grains than those detected at 1.3 mm measurements. (Greaves et al., in prep.)

sizes, is readily studied by determining the slope of the spectral energy distribution (SED) of the dust thermal emission at submillimeter and millimeter wavelengths. The dust mass opacity index at wavelengths longer than 0.1 millimeter is approximately a power-law whose normalization depends on the dust properties, such as composition, size distribution, and geometry (Draine 2006). The index of the power law is commonly given by β . The presence of large grains is detectable through a decrease in β , which can be derived directly from the slope of the Rayleigh-Jeans tail of the SED, α , where $\beta = \alpha - 2$ when the emission is optically thin. Numerous studies have revealed that the β values of disks are substantially lower than the typical ISM value of ~ 2 (e.g., Testi et al. 2003; Weintraub et al. 1989; Adams et al. 1990; Beckwith et al. 1990; Beckwith & Sargent 1991; Mannings & Emerson 1994).

The key stumbling block to the interpretation of β occurs when the disk is not resolved spatially. The amount of flux detected at a given wavelength is a function of both β and the size of the disk (Testi et al. 2001). Resolving the ambiguity therefore is truly a matter of resolution, and sufficient resolution is only offered at these wavelengths by interferometers.

Among the three high level science goals of ALMA is the ability to detect and image gas kinematics in protoplanetary disks undergoing planetary formation at 150 pc. At ALMA’s observing wavelengths, its capability for imaging the continuum dust emission in these disks is also second-to-none. At present, however, the longest wavelength that ALMA can reach is 3.6 mm. Given that dust particles emit very inefficiently at wavelengths longer than their sizes, the present ALMA design will not be sensitive to particles larger than ~ 3 mm. *This situation negates ALMA’s potential ability to follow the dust grain growth from mm-sized to cm-sized pebbles in protoplanetary disks.*

Figure 2 shows the SEDs for three different circumstellar disk models, computed using the full dust radiative transfer MCFOST code (Pinte et al. 2006; Pinte et al. 2009). The model parameters are representative of protoplanetary disks (although there is substantial object-to-object variation). The circumstellar disk is passively heated by a 4000 K, $2 L_{\odot}$ central star and the system is located 160 pc away. The dust component of the disk is assumed to be fully mixed with the gas and the latter is assumed to be in vertical hydrostatic equilibrium. The disk extends radially from 1 AU to 100 AU. The total dust mass in the model is $10^{-3} M_{\odot}$ (the gas component is irrelevant for continuum emission calculations, so its mass is not set in the model, though a typical 100:1 gas:dust ratio is generally assumed). The dust population is described by a single power-law size distribution $N(a) \propto a^{-3.5}$ with a minimum grain size of $0.03 \mu\text{m}$ and extending to $10 \mu\text{m}$, 1 mm or 1 cm depending on the model. The dust composition is taken to be the “astronomical silicates” model from Draine (2003).

Figure 2 reveals that observations in the ALMA Band 1 spectral region are crucial for

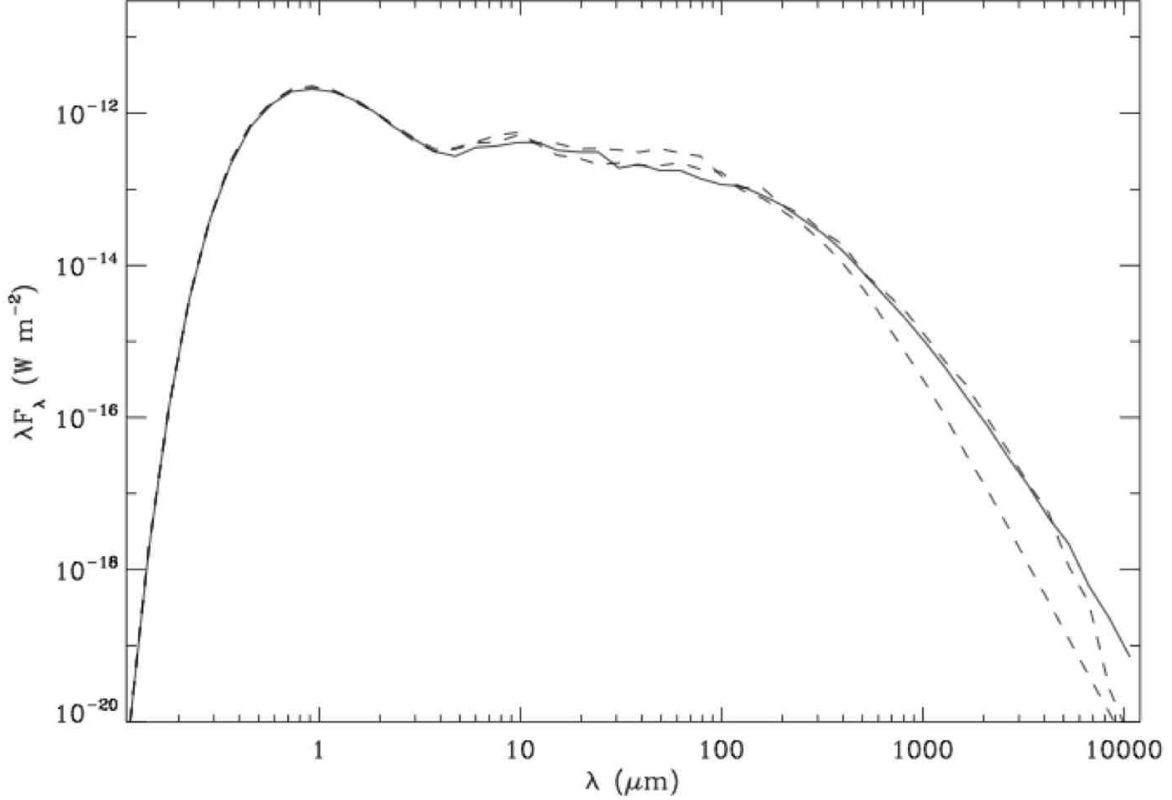


Fig. 2.— Spectral energy distribution plot showing the differences between three disk models having different maximum grain sizes. The solid curve is the model with $a_{\text{max}} = 1$ cm, which keeps declining with roughly constant slope all the way to 1 cm. The two dashed curves are for $a_{\text{max}} = 10$ μm and 1 mm. The top one, which breaks around 5 mm is the model with $a_{\text{max}} = 1$ mm. It’s interesting to note how the fluxes are very much the same for $a_{\text{max}} = 1$ mm or 1 cm, except precisely towards ALMA’s Band 1. There is at least an order of magnitude difference in power at 1 cm between the $\text{max}_{\text{size}} = 1$ mm versus the $\text{max}_{\text{size}} = 1$ cm disks. These models indicate that observations at the ALMA Band 1 regime are crucial for determining whether grain-growth to cm-sizes is indeed occurring.

determining whether grain-growth to cm-sizes is indeed occurring. The 1 cm flux density of the $\text{max}_{\text{size}}=1$ cm disk model is $\sim 50 \mu\text{Jy}$, comparable to the 1σ sensitivities provided by ALMA’s Band 1 with 1 minute integration. Besides ALMA, there are no existing or planned southern astronomical facilities capable of observing to such depths at these frequencies. Therefore, *if ALMA Band 1 receivers are not built there will be no way of putting ALMA observations of protoplanetary disks in the context of coagulation of dust grains to centimeter sizes.* Though such information could be acquired in part with the JVLTA (for sufficiently northern sources), ALMA Band 1 receivers would yield superior data for comparison with those of other Bands, given greater similarities in spatial frequency coverage. (Spatial frequency coverage depends on the latitude of the observatory and the declination of the source.)

By complementing observations in other ALMA Bands, Band 1 will provide a crucial longer wavelength lever to minimize the uncertainty in α . Evidence for small pebbles has been detected in several disks (Rodmann et al. 2006). The prime example is TW Hya, a protoplanetary disk 50 pc from the Sun (Wilner et al. 2000). Its SED is well matched by an irradiated accretion disk model fit from 10s of AU to an outer radius of 200 AU and requires the presence of particle sizes up to 1 cm in the disk (see Figure 3). The measured β is 0.7 ± 0.1 (Calvet et al. 2002). To date, no trend in β has been detected with stellar luminosity, mass or age (Ricci et al. 2010). Lower α values are associated with less 60 μm excess, however, suggesting that settling or agglomeration processes could be removing the smallest grains, decreasing the shorter wavelength emission (Acke et al. 2004). (See §6.1.1 for further discussion of probes of small grains with the ALMA Band 1 receivers.)

At the resolution provided by its longest baselines at ~ 40 GHz ($\sim 0.14''$), ALMA will easily resolve protoplanetary disks at the distance of the closest star-forming regions (50–150 pc). These resolved images will provide the most accurate determination of the disk’s dust mass. The dust distribution at centimeter wavelengths can then be compared to millimeter and submillimeter images, revealing where in the disk dust coagulation is occurring. For example, previous investigations of the radial dependency of dust properties in disks by Guilloteau et al. (2009) and Isella et al. (2010) were conducted at 1 mm and 3 mm, and as such they were sensitive to only millimeter-sized grains. Note, however, that Melis et al. (2011) used the Jansky VLA to map the 7 mm emission from the protoplanetary disk around the young source L1527 IRS at $\sim 1.5''$ and tentatively detected a *dearth* of “pebble-sized” grains. ALMA Band 1 receivers will help clarify this situation. As described above, Band 1 data will be sensitive to larger grains. Moreover, through detection of concentrations of such large grains, protoplanets in formation can be identified. These condensations are predicted by simulations of gravitational instability models (see Figure 4a; Greaves et al. 2008) and have been detected in the nearby star HL Tau (Figure 4b; Greaves et al. 2008).

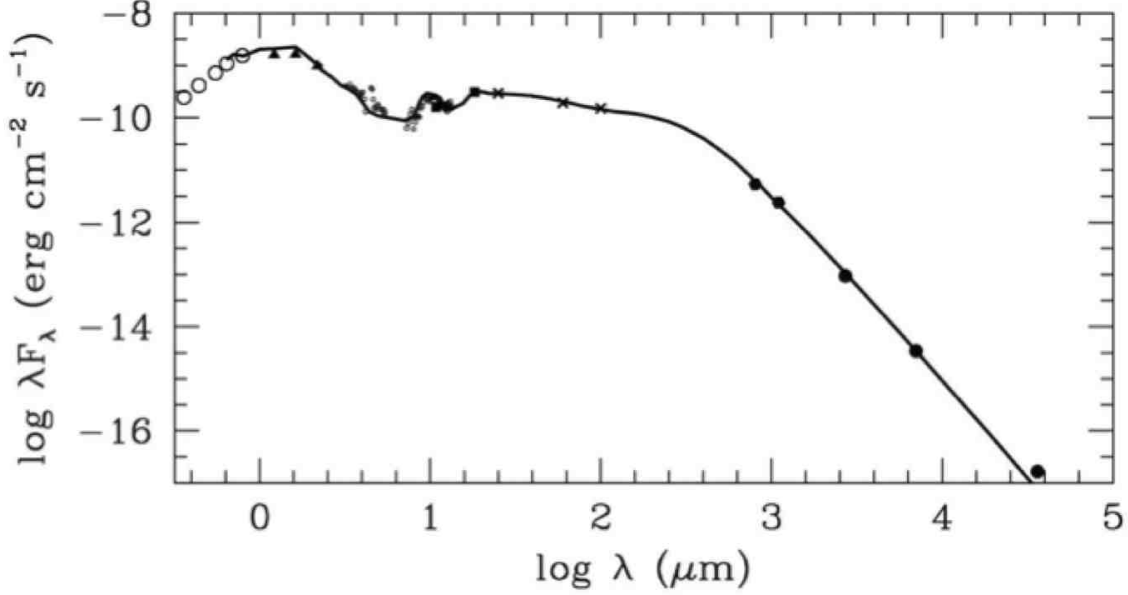


Fig. 3.— Spectral energy distribution of TW Hya, showing the fit to the SED for an irradiated accretion disk model with a maximum particle size of 1 cm (Calvet et al. 2002).

Detecting dust emission at centimeter wavelengths also requires high sensitivity, because its brightness is several orders of magnitude lower than in the submillimeter. In addition, at wavelengths longer than 7 mm (i.e., $\nu < 45$ GHz), the contribution from other radiative processes, such as ionized winds, can contribute significantly to the total flux and complicate the interpretation of detected emission. Rodmann et al. (2006) found that the contribution of free-free emission to the total flux is typically 25% at a wavelength of 7 mm. Observations of continuum emission at the 35–50 GHz (6–9 mm) spectral range enabled by Band 1 would increase substantially the sampling rate in the region where emission is detected from both the free-free and thermal dust emission components. The synergy with the JVLA will provide a longer wavelength lever for sources observed in common, providing an estimate of the free-free contribution to the Band 1 flux. Such data would not be essential, however, given wide frequency coverage within Band 1 alone. For example, multiple continuum observations could be used to quantify accurately the relative amounts of free-free and dust emission through changes in spectral slope, and thereby determine precisely the contribution from large dust grains (i.e., protoplanetary material).

In summary, ALMA Band 1 receivers would provide the sensitivity to long wavelength emission needed to probe dust coagulation and growth in protoplanetary disks observed at higher-frequency bands. Of course, ALMA Band 1 will allow such investigations of sources

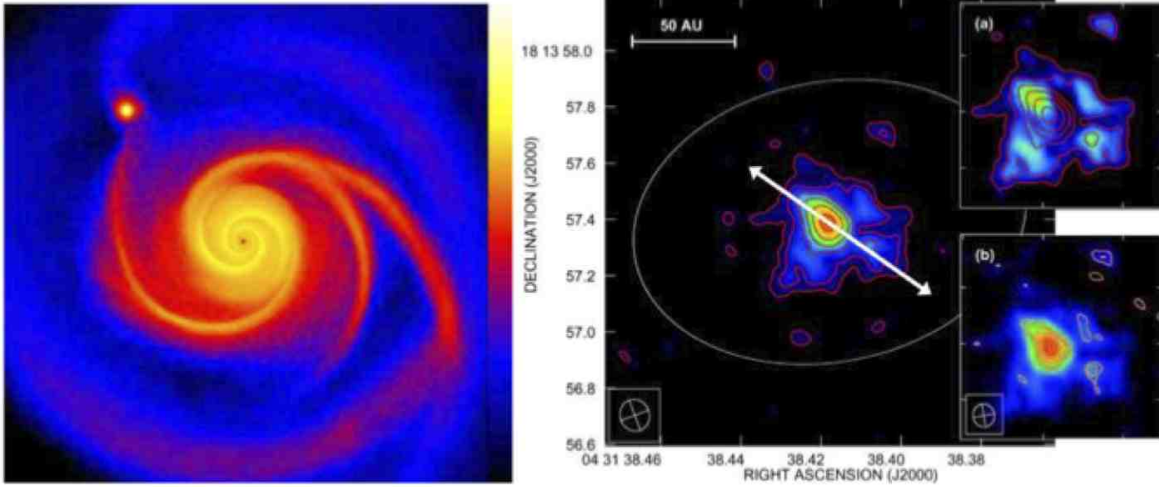


Fig. 4.— (Left) Image from an SPH simulation showing the surface density structure of a $0.3 M_{\odot}$ disk around a $0.5 M_{\odot}$ star. A single dense clump has formed in the disk, at a radius of 75 AU and with a mass of $\sim 8 M_{\text{Jup}}$. (Right) VLA 1.3 cm images toward HL Tau. The main image shows natural weighting with a beam of $0.11''$ FWHM. The arrow indicates the jet axis. Upper inset: compact central peak subtracted. Lower inset: uniform weighting, with a beam of $0.08''$ FWHM. The compact object lies to the upper right hand side. This condensation was also detected at 1.4 mm with the BIMA array (Welch et al. 2004).

too far south to observe with the JVLA. (For the highest resolutions, the improved phase stability available at ALMA will also be very important.) Furthermore, as comparisons with higher frequencies are better when there is similar spatial frequency coverage, however, sources are best observed at different wavelengths from the same latitude, favouring ALMA data over JVLA data even for northern sources.

4.1.2. Debris Disks

Around main sequence stars, pebble-sized bodies are produced differently than in disks around pre-main-sequence stars. Here, destructive collisional cascades from even larger planetesimals through to centimeter, millimeter, and then micron-sized particles provides ongoing replenishment of the debris population (Wyatt 2009; Dullemond & Dominik 2005). The methods for detecting large (i.e., centimeter-sized) grains is the same as in protoplanetary disks, despite their origin in destructive rather than agglomerative processes. In each case, the longer the wavelength at which continuum emission is detected, the larger the grains

that must be present in the system.

Using ALMA Band 7, Boley et al. (2012) detected the debris disk of Fomalhaut, and noted its sharp inner and outer boundary. Band 1 images, however, could show higher contrast features in debris disks compared to other ALMA Bands, due to the longer resonant lifetimes of the larger particles that dominate the emission. This sensitivity in turn will help detect any edges and gaps in the disks. Dramatic changes in the morphology of debris disks as a function of wavelength have already been observed (e.g., Maness et al. 2008), but not yet at the long wavelengths Band 1 will probe. When observed, such structures are often considered signposts to the existence of planets.

Detections of debris disks in Band 1 will be challenging compared to detecting forming condensations in protoplanetary disks. Debris disks typically have relatively low surface brightnesses and large spatial distributions 100s of AU in radii. They also can be found much closer to the Sun than the nearest protoplanetary disks. Indeed, the closest disks could subtend as much as $\sim 150''$ on the sky (assuming a 300 AU diameter disk at 2 pc). Therefore, ALMA’s large field-of-view relative to other long wavelength instruments, such as the JVLA, will be very advantageous for imaging these objects. (Mosaicking will still be required to image the largest ones on the sky.) In addition, the ALMA 12-m Array’s smaller minimum baselines and the ACA will provide higher sensitivity to the low surface brightness emission from these objects.

4.2. The First Generation of Galaxies: Molecular gas in galaxies during the era of re-ionization

The first generation of luminous objects in the Universe began the process of re-ionizing the intergalactic medium (IGM). The detection of large-scale polarization in the cosmic microwave background (CMB), caused by Thomson scattering of the CMB by the IGM during re-ionization, suggests that the Universe was significantly ionized as far back as $z \approx 11.0 \pm 1.4$ (Dunkley et al. 2009). The “near” edge of the era of re-ionization has been inferred from the detection of the Gunn-Peterson effect (Gunn & Peterson 1965) toward galaxies with $z \gtrsim 6$ (Fan et al. 2006a,b). The nearly complete absorption of all continuum shortward of the $\text{Ly}\alpha$ break is due to moderate amounts of neutral hydrogen in the IGM, suggesting re-ionization was complete by $z \approx 6$. The Gunn-Peterson effect also insures that at these redshifts the Universe is opaque at wavelengths shorter than $\sim 1 \mu\text{m}$.

To study the first generations of galaxies, and to understand the origins of the black hole-bulge mass relation, it will be necessary to study the star-formation properties of galaxies

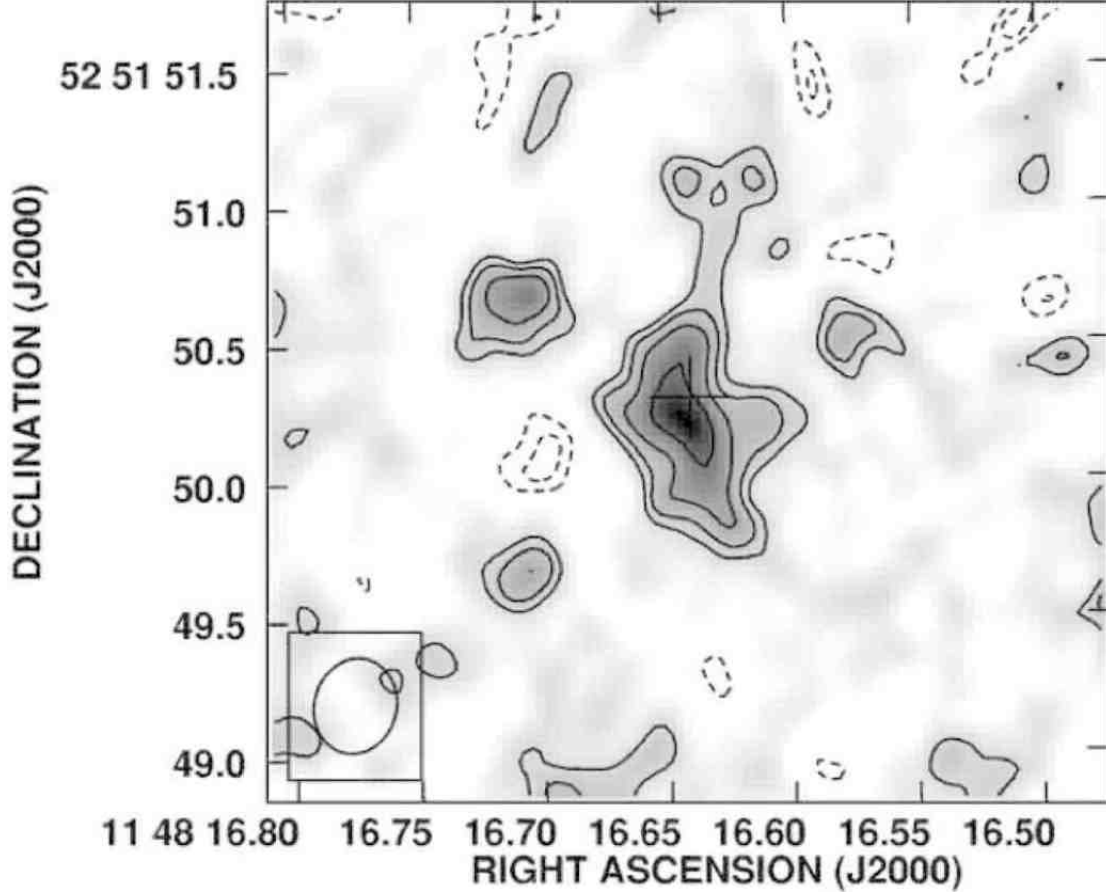


Fig. 5.— VLA redshifted CO $J=3-2$ map of the quasar J1148+5251 using the combined B- and C-array data sets (covering the total bandwidth, 37.5 MHz or 240 km s⁻¹), from Walter et al. (2004). Contours are shown at $-2, -1.4, 1.4, 2, 2.8,$ and $4 \times \sigma$ ($1 \sigma = 43 \mu\text{Jy beam}^{-1}$). The beam size ($0.35'' \times 0.30''$) is shown in the bottom left corner; the plus sign indicates the SDSS position (and positional accuracy) of J1148+5251.

in the $6 \lesssim z \lesssim 11$ range. Quasar hosts and other sources are rapidly being discovered at the near end of this range (e.g., Cool et al. 2006; Mortlock et al. 2008; Glikman et al. 2008; Willott et al. 2009), and searches are underway for even more distant objects (e.g., Ota et al. 2008; Bouwens et al. 2009).

Recently, CO has been detected¹ in galaxies at redshifts >6 . These and other observations in the cm/mm of $z > 6$ galaxies are summarized by Carilli et al. (2008; see also the large surveys of CO at $z > 6$ by Wang et al. 2010, 2011a and references therein). Current instrumentation sensitivities are such that detections are limited to hyperluminous infrared galaxies, i.e. $L_{\text{FIR}} > 10^{13} L_{\odot}$. Only a small fraction of galaxies are this luminous. The best-studied such object is J1148+5251 with a redshift of $z = 6.419$ (see Carilli et al. 2008). For example, Walter et al. (2004) imaged the CO $J=3-2$ emission (Figure 5) using the VLA, from which they were able to infer the dynamical mass. Walter et al. (2009) were not able to detect the [NII] line at $205 \mu\text{m}$, but did detect the CO $J=6-5$ transition. More recently, Wang et al. (2011b) detected the lower-energy CO $J=2-1$ transition and Reichers et al. (2009) imaged CO $J=7-6$ and CI ($^3P_2-^3P_1$) emission towards this source. These and other (dust continuum) observations show that there was already a significant abundance of metals and dust by this epoch.

Figure 6 shows the observable frequency of rotational transitions of ^{12}CO , from $J=1-0$ through $J=10-9$, as a function of redshift. Also shown are the frequency ranges of the ALMA Bands (excluding Band 2 for clarity). Note that this Figure shows the new nominal range of Band 1 of 35-50 GHz, as this range will yield the highest sensitivities. As the Figure shows, Band 1 receivers will be able to detect galaxies in $J=3-2$ at $6 \lesssim z \lesssim 9$, i.e., in the redshifts of the era of re-ionization ($z \gtrsim 6$), while higher Bands can only observe higher- J lines that may be less excited. (For example, Band 3 receivers would be able to detect $J=6-5$ emission in the range $4.8 \lesssim z \lesssim 7.2$.) Moreover, Band 1 receivers will enable coverage for $J=2-1$ and $J=1-0$ emission at $3.6 \lesssim z \lesssim 5.6$ and $1.3 \lesssim z \lesssim 2.3$, respectively. Assuming a $150 \mu\text{Jy}$ CO $J=2-1$ line of width $\sim 600 \text{ km s}^{-1}$ at $z = 5.7$, a 5σ detection would take less than 4 hours with the 50-antenna ALMA 12-m Array.

Band 1 will also allow multiline observations toward certain subsets of redshifts. For example, galaxies at $1.3 \lesssim z \lesssim 2.3$ can be observed in Band 1 but also at $J=4-3$ and $J=3-2$ in Band 4 (NB: a small gap exists at $z \approx 1.8$). Figure 6 also shows that in addition the [CII] $^2P_{3/2}-^2P_{1/2}$ line can be observed toward a subset of these galaxies at $1.6 \lesssim z \lesssim 2.2$ using

¹Note that interferometers in general have an advantage over single-dish telescopes when detecting molecular emission at high redshift since their high-resolution imaging capabilities provide the spatial information needed to associate a detection with a specific object.

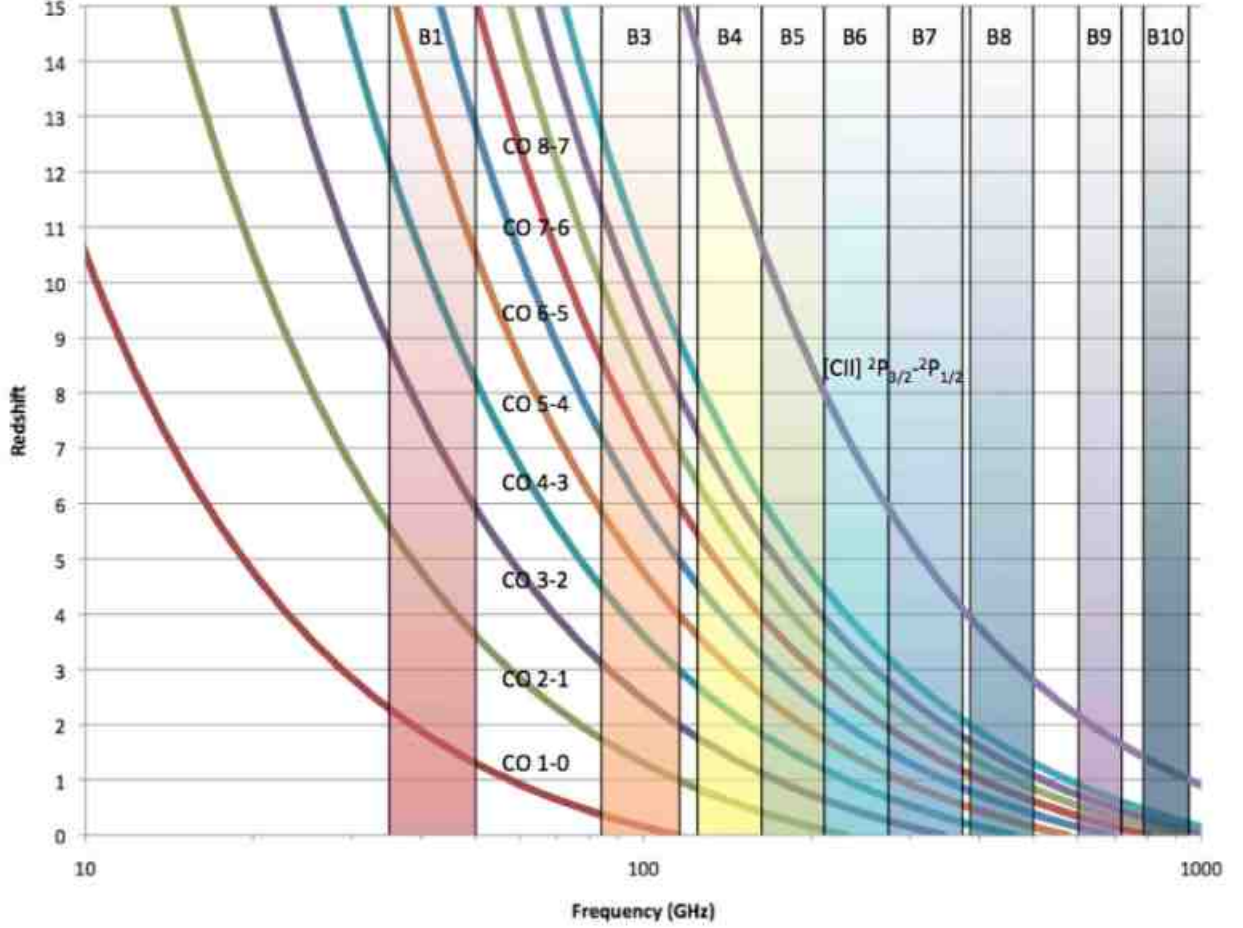


Fig. 6.— Observable frequencies of ^{12}CO rotational transitions and $[\text{CII}] \ ^2\text{P}_{3/2} - ^2\text{P}_{1/2}$ as a function of redshift. The frequency ranges of the ALMA Bands are also shown. Note that the range for Band 1 reflects the new nominal range of 35-50 GHz.

Band 9. The [CII] line can also be observed toward galaxies at $2.8 \lesssim z \lesssim 5.9$ using Bands 7 and 8 (NB: a small gap in redshift coverage exists at $z \approx 4$).

As with other ALMA Bands, high-redshift science will be done with Band 1 in a targeted mode, i.e., towards known high- z sources. An instantaneous ~ 8 GHz range of frequency coverage, however, will allow significant sensitivity to other sources proximate on the sky to the known target source but at quite different redshifts. (If the target sources are within clustered environments, other sources may even be found at similar redshifts.) Indeed, “blank-sky” surveys, made by pointing ALMA towards one location but stepping through the entire Band 1 frequency range, are an enticing possibility (see, e.g., Aravena et al. 2012). In particular, the ALMA 12-m Array’s antennas provide a much larger instantaneous field-of-view than the JVLA’s antennas, allowing wider searches of blank sky.

In summary, ALMA Band 1 will allow for wide-band observations of molecular emission from many interesting galaxies in the era of re-ionization. Band 1 allows for observations of lower- J lines that are complementary to lines detected with higher frequency bands. In particular, ALMA’s southern location will allow observations of objects not observable (well or at all) with the JVLA. Also, its larger field-of-view gives it an edge in areal “blank sky” coverage for detecting at similar or different redshifts sources proximate to known targets.

4.2.1. Quasar Host Galaxies

The discovery of molecular gas in quasar host galaxies at $z \sim 6$, when the Universe was less than 1 Gyr old (Walter et al. 2003; Bertoldi et al. 2003; Carilli et al. 2007), has opened a new window on the study of gas in systems that contributed to the re-ionization of the Universe. Studies of how the molecular gas properties should evolve, and how they can be used to reveal the dynamics of these *massive* systems, have recently prompted a new generation of semi-analytic models with the further aim of understanding how high-redshift quasars fit within the context of large-scale structure formation. Li et al. (2007, 2008) have used state of the art N-body simulations to show that the observed optical properties of high-redshift quasars can be explained if these objects formed early on in the most massive dark matter halos ($\sim 8 \times 10^{12} M_{\odot}$). These models predict that the most luminous quasars should evolve due to an increase of major mergers, which one would expect to find evidence for in the CO line profiles and the spatial distribution of the molecular gas (Narayanan et al. 2008). Detailed radiative transfer models of the FIR spectral energy distribution of these systems have been driven by the observations of one $z = 6.42$ quasar (namely J1148+5251; Walter et al. 2003, 2004). Larger samples of CO-detected quasars are needed to provide better constraints on the models and constrain dynamical masses to compare

with infrared measurements of black-hole masses (e.g., from MgII lines) and explore the (possible) evolution of the relation between the masses of central black holes and bulges. Current 3 mm surveys of high- J CO line emission in $z \sim 6$ FIR-luminous quasars are being conducted with the PdBI, having successfully detected CO line emission in eight objects (Wang et al. 2010, 2011a). Lower- J lines, like those accessible with ALMA Band 1, will trace the more abundant lower density gas in these systems. Here again, ALMA’s southern location will prove to be an advantage for targets too far south to be well observed with the JVLA.

4.2.2. *Lyman- α Emitters*

The rarity of the luminous quasars at early times suggests that their UV emission was unlikely to have contributed significantly to the re-ionization of the Universe (e.g., Fan et al. 2001). A more important type of galaxy in the context of cosmic re-ionization are the Lyman- α emitters (hereafter LAEs). These galaxies were discovered through their excess emission in narrow-band images centered on the redshifted Lyman- α line (e.g. Hu et al. 1998; Rhoads et al. 2000; Taniguchi et al. 2005), and constitute a significant fraction of the star-forming galaxy population at $z \sim 6$. While the star-formation rates in LAEs inferred from their UV continuum emission are a few tens of solar masses per year (e.g., Taniguchi et al. 2005), their number density and the shape of the Lyman- α emission line provide important probes of physical conditions in the Universe around the epoch of re-ionization. As such, it is very important that we understand the properties related to their star-formation activity. In particular, we need to quantify the amount of molecular gas available for fuel. Wagg, Kanekar & Carilli (2009) used the Green Bank Telescope to search for CO $J=1-0$ line emission in two $z > 6.5$ LAEs, including the highest spectroscopically confirmed redshift LAE at $z = 6.96$ (Iye et al. 2006). The limits to the CO line luminosity implied by the non-detections of CO $J=1-0$ in these two objects suggest modest molecular gas masses ($\lesssim 10^{10} M_{\odot}$). This conclusion, however, is based on observations of only two objects, and future studies would benefit from the sensitivity gained by observing higher- J CO transitions, whose flux density may scale as ν^2 due to a contribution to the molecular gas excitation by the cosmic microwave background radiation (19 K at $z = 6$). With other facilities, it has been proven challenging to detect even the higher energy CO $J=2-1$ line from Lyman- α -emitting galaxies at these redshifts, using existing facilities (Wagg & Kanekar 2011). At these redshifts, such studies would require ALMA, including the Band 1 receivers. Again, ALMA’s southern location is advantageous for the detection of more southern LAEs.

5. Suitability of Band 1 for ALMA vs. JVL A

Here we compare the relative capabilities of ALMA and the Jansky Very Large Array (JVLA) over Band 1 frequencies in common. The JVLA currently has observing capability over the nominal Band 1 frequency range of 35–50 GHz, through its receivers in the K_a-band (26.5–40 GHz) and Q-band (40–50 GHz). ALMA Band 1, however, will likely be extended to 50–52 GHz, frequencies the JVLA cannot observe. In the following, we compare the differences in site conditions and array characteristics that show that Band 1 observing is superior with ALMA than with the JVLA.

5.1. Site Conditions

ALMA is located on the Llano de Chajnantor at a higher altitude (5040 m) than the JVLA on the Plains of San Agustin (2124 m). Opacity in Band 1 consists of a wet component of atmospheric water vapor and a dry component of non-H₂O gases, like O₂. The quantity of the wet component, as measured by precipitable water vapor (PWV) affects more the lower end of the Band 1 frequency range. The dry component, however, dominates at the upper end. Nevertheless, the ALMA site is very well-suited for Band 1 observing. Even during the worst octile of weather, however, the typical optical depth through the Band 1 Receiver range is less than 0.1. Though other frequency ranges like Band 3 can still use such weather, the addition of cloud cover and water droplets in the air make even lower frequency observations more attractive.

The PWV over the JVLA during the years 1990–1998 was measured to range between 4.5 mm in winter and 14 mm in summer with a ± 2 mm scatter throughout the year (Butler 1998; VLA Memo 237). In comparison, the PWV over ALMA during the years 1995–2003 was measured to range between 1.2 mm in winter to 3.5–7.0 mm in summer (median ≈ 1.4 mm), using opacity data obtained by Otórola et al. (2005; ALMA Memo 512) and conversions provided by D’Addario & Holdaway (2003; ALMA Memo 521). For frequencies <45 GHz, Butler (2010; VLA Test Memo 232) found empirically a linear relation between opacity and PWV, where opacities varied from 6% to 10% from 1 mm to 14 mm. Assuming this relation is applicable to both observatories, we find the atmospheric opacities at <45 GHz over ALMA to be generally half those over JVLA.

Phase stability over the JVLA was measured with a 300-m baseline test interferometer at 11.3 GHz, and median characteristics from one year of data were reported by Butler & Desai (1999; VLA Test Memo 222). They found median phase variation rms values ranging from 2–2.5° in winter nighttime to >10° in summer daytime. Scaling these values to the

zenith and converting to path delay rms fluctuations, these phases convert to 430-540 fsec to 2100 fsec, respectively. For ALMA, D’Addario & Holdaway, using six years of data from a similar 300-m baseline test interferometer, determined a median path delay fluctuation of 500 fsec. (A seasonal breakdown was not provided.) Though the data are somewhat scant, the overall median path delay at ALMA is about equal that of the best median path delays at the JVLA in winter nighttime. Note, however, that phase stability can be mitigated by water vapor radiometer data available at both sites.

5.2. Array Characteristics

The most important difference between the characteristics of ALMA and the JVLA is that they are located at very different latitudes, the former at -23° and the latter at $+34^\circ$. Some sources too far south to be observed at the JVLA (or at least observed well) will be observable with ALMA. (The Australia Telescope Compact Array (ATCA) can also observe some Band 1 frequencies from the southern hemisphere but at much lower relative sensitivity than ALMA or the JVLA. Hence, we do not consider it further.) Important targets in the southern hemisphere that are better observed at ALMA than the JVLA (if at all) include Sgr A*, the center of our Galaxy, the Magellanic Clouds, the closest neighboring galaxies, and TW Hya, the closest protoplanetary disk. Indeed, any source observed with ALMA in higher frequency bands can be more effectively observed at 35-50 GHz with Band 1 receivers. Also, with numerous satellite observatories providing full sky coverage (e.g., JWST, *Spitzer*, *Herschel*), having full-sky coverage from ground-based facilities at important frequencies is optimal.

Table 1 summarizes the differences between ALMA and the JVLA. Comparing their attributes, we note that ALMA’s 12-m Array has antennas of smaller surface area than those of the JVLA (12-m diameter vs. 25-m) but these are larger in number (50 in the 12-m Array vs. 27) and have higher pointing accuracies ($0.6''$ vs. $2-3''$) and aperture efficiencies at Band 1 frequencies (0.78 vs. 0.34–0.39). Combining these numbers (except pointing accuracy), the effective surface area of the ALMA 12-m Array is a factor of 0.85–0.98 that of the JVLA. Adding Band 1 to the ACA antennas would minimize even this small difference. ALMA has the same 8 GHz maximum bandwidth as the JVLA with its new WIDAR correlator. ALMA’s present correlator has a lower maximum spectral resolution than the JVLA’s, however, i.e., a maximum of 3.82 kHz vs. 1 Hz, respectively. (ALMA’s correlator of course could be similarly upgraded in the future.)

Given differing antenna numbers, sizes, and baselines, the two observatories differ in

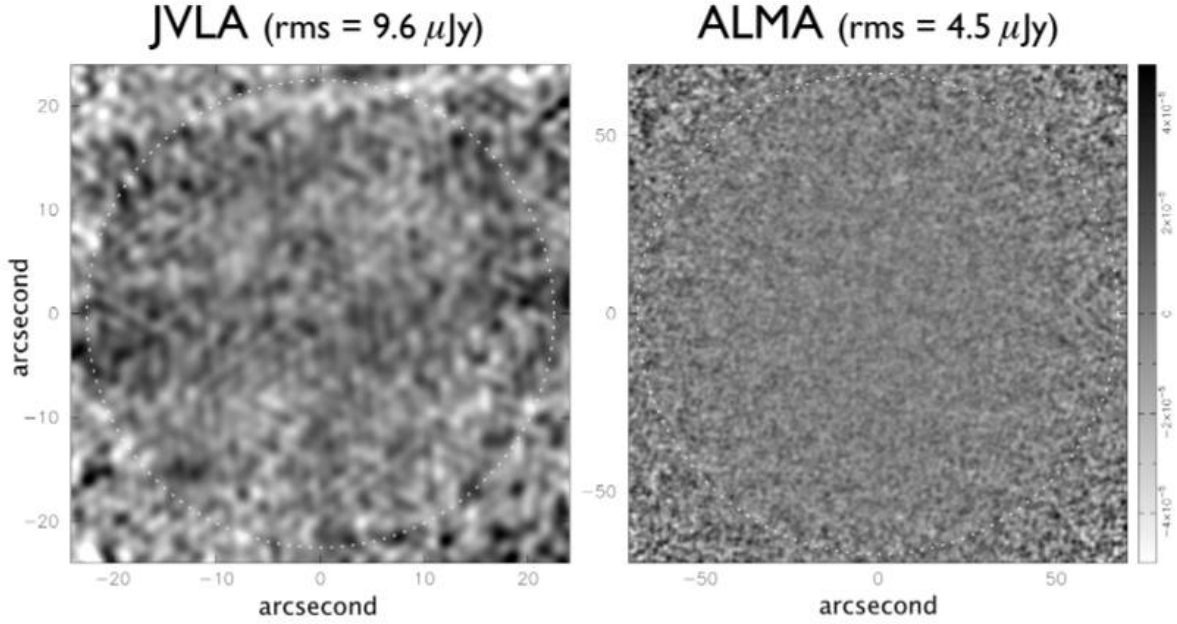


Fig. 7.— Images from JVLA and ALMA observations simulated with CASA. The observations were set toward a “blank” sky at 45 GHz with 8 GHz (continuum) bandwidth, with JVLA in its D-configuration while ALMA in its “12” configuration provided in CASA. Both array configurations give rise to a similar angular resolution of $\sim 1''.6$ FWHM. The white dotted circles denote the corresponding primary beam sizes. The resulting 1σ rms noise levels after 2 hours of on-source integration are $9.6\ \mu\text{Jy}$ and $4.5\ \mu\text{Jy}$, respectively, for JVLA and ALMA, which are in general agreement with the estimated noise level shown in Table 2.

Table 1: Summary of general properties of the ALMA Band 1 and JVL A

	ALMA	
	Band 1	JVLA
Latitude	-23°	$+34^\circ$
Altitude (m)	5040	2124
No. of antennas	50	25
Antenna diameter	12	25
Pointing accuracy (arcsec)	0.6	2–3
Frequencies (GHz)	35–52	26.5–40 (band K _a) 40–50 (band Q)
Aperture efficiency, A_e	0.78	0.34–0.39
$\Delta\nu_{\max}$ (Hz)	3820	1
Single-field sensitivity ($\propto ND^2$)	7200	17000
<i>effective</i>	5600	5800–6600
Mosaic image sensitivity ($\propto ND$)	600	680
<i>effective</i>	530	420–390
Image fidelity ($\propto N^3$)	130000	20000

various imaging metrics²:

- Comparing the face-value “single-field sensitivity” metric (ND^2 ; where D is the antenna diameter and N is the number of antennas), ALMA appears about half as “sensitive” as the JVLA (7200 vs. 17000). Factoring in aperture efficiencies to give effective values of D , however, the metrics are actually much more similar (5600 vs. 5800–6600). Table 2 provides more realistic comparisons of JVLA and ALMA sensitivities for point sources across the proposed Band 1 frequency range, estimated using their respective sensitivity calculators³. Note that the JVLA sensitivities require the JVLA’s best

²These metrics were defined and used to compare ALMA to other existing interferometers in the 2005 NRC document *The Atacama Large Millimetre Array: Implications of a Potential Descope*.

³For JVLA and ALMA, see <https://science.nrao.edu/facilities/evla/calibration-and-tools/exposure> and <http://almascience.eso.org/call-for-proposals/sensitivity-calculator>, respectively. For these calculations, we assume the original ALMA specifications for Band 1 receiver performance, i.e., the same 40–80 K as for the JVLA’s K_a/Q-band receivers.

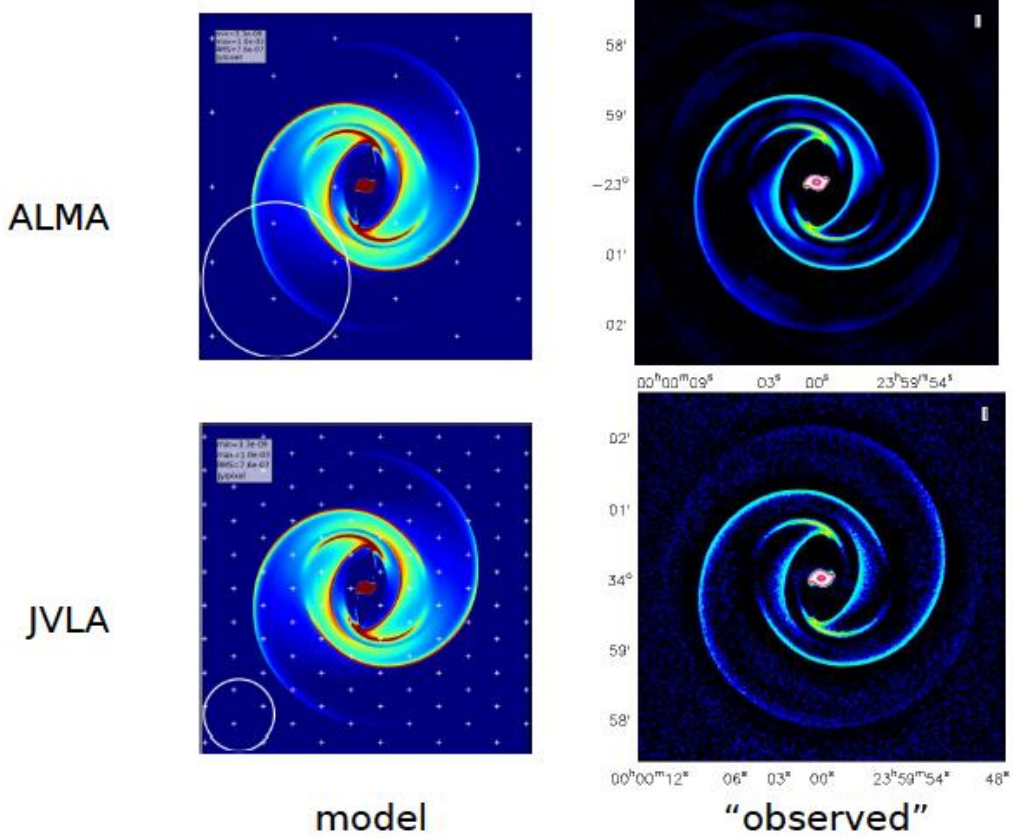


Fig. 8.— Images from CASA simulations of JVLA and ALMA mosaic observations of 45 GHz continuum. The left-hand panels show the model image convolved with the synthesized beams. The pointing patterns for the mosaicked observations are shown with white dots. The right-hand panels show the resulting observed images. Both simulated observations are executed with eight hours of on-source time in total toward the zenith. The ALMA and JVLA were assumed to be in their “12” and “D” configurations, (both provided in CASA), respectively, which resulted in similar synthesized beam sizes of $1.7'' \times 1.7''$. The achieved noise level by ALMA is around three times better than that by JVLA. (i.e., $10 \mu\text{Jy beam}^{-1}$ for ALMA vs. $30 \mu\text{Jy beam}^{-1}$ for JVLA). Observation overheads (e.g., calibration scans) and phase decoherence due to site location were not included in the simulations, both of which will lead to greater degradation in the JVLA images.

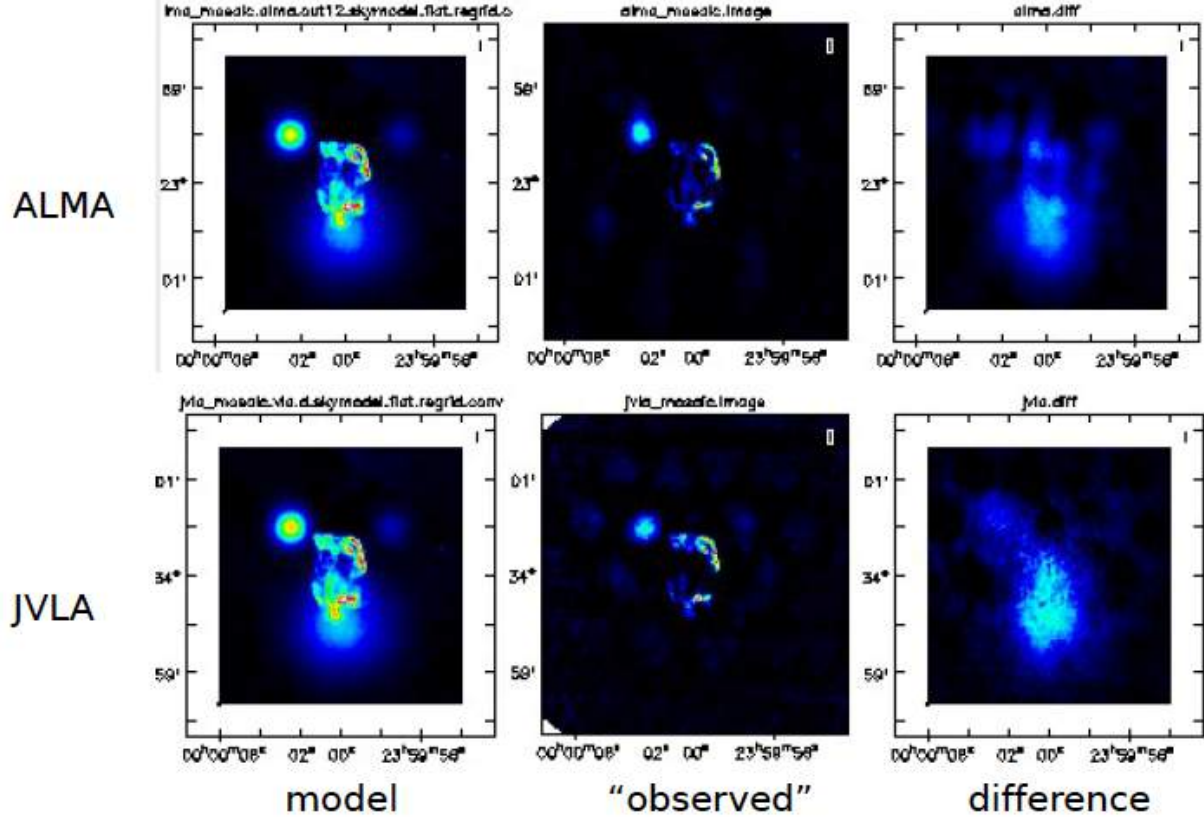


Fig. 9.— Images from CASA simulations of observations of extended 45 GHz emission with the JVLA and ALMA. The left-hand panels show the model image (a superposition of the G41.1-0.3.b template provided by the CASA guide with three extended Gaussian sources (two $18''$ in size and one $48''$ in size) convolved with the synthesized beams. The middle panels show the resulting images from the simulations. The right-hand panels show the difference between the model and observation images. Both simulated observations were executed with one hour of on-source time in total toward the zenith. The ALMA and JVLA are assumed to be in their “12” and “D” configurations (both provided in CASA), respectively, which resulted in similar synthesized beam sizes of $1.7'' \times 1.7''$. The achieved noise level by ALMA is around five times better than that by JVLA (i.e., $10 \mu\text{Jy beam}^{-1}$ for ALMA vs. $50 \mu\text{Jy beam}^{-1}$ for JVLA). Observation overheads (e.g., calibration scans) and phase decoherence due to site location were not included in the simulations, both of which will lead to greater degradation in the JVLA images.

Table 2: Comparison of Point-Source Sensitivity between JVLA and ALMA

		JVLA		ALMA	
no. of antennas		25		50	
polarization		dual		dual	
weather		winter		auto (5.2 mm) PWV	
source position		zenith		zenith	
on-source time		60 s	1 hr	60 s	1 hr
bandwidth		1 MHz		1 MHz	
freq.	35 GHz	3.2 mJy	0.41 mJy	3.0 mJy	0.38 mJy
	40 GHz	3.6 mJy	0.47 mJy	3.1 mJy	0.40 mJy
	45 GHz	5.1 mJy	0.68 mJy	3.6 mJy	0.47 mJy
	50 GHz	25.5 mJy	3.29 mJy	(not available)	
bandwidth		8 GHz		8 GHz	
freq.	40 GHz	50 μ Jy	5.4 μ Jy	35 μ Jy	4.5 μ Jy
	45 GHz	78 μ Jy	10 μ Jy	41 μ Jy	5.3 μ Jy

weather (“winter”) while a relatively high PWV level (5.2 mm) was actually chosen for ALMA here. From these calculations, we see continuum sensitivities of ALMA for Band 1 are actually *similar to better* than those of the JVLA. For example, a 1σ rms of $\sim 5\ \mu\text{Jy beam}^{-1}$ is expected at 40 GHz after 1 hour of integration at both observatories. At higher frequencies (e.g., >45 GHz), however, the point source sensitivity of ALMA is *better* than that of JVLA by factors of 1.4–1.9, depending on bandwidth. (Simulations of JVLA and ALMA observations suggest even larger improvements; see below.) In addition, Figure 7 shows simulated “blank-sky” observations at 45 GHz carried out with CASA, giving another perspective on this comparison. (ALMA’s improved pointing accuracy and better phase stability were not fully incorporated into these calculations.) Note also that ALMA’s 12-m diameter antennas provide a field-of-view for single-pointing observations that is more than twice as wide as what the JVLA’s 25-m diameter antennas provide (see Table 3), so ALMA’s similar or better sensitivity is obtained over a wider area in a single pointing.

- Comparing the “mosaic image sensitivity” metric (ND), again on face value, ALMA’s 12-m Array and the JVLA appear already quite similar (600 vs. 680, respectively). Factoring in only the improved aperture efficiencies of ALMA at its lowest frequencies vs. those of the JVLA at its highest frequencies, the comparison is in ALMA’s favour by a factor of ~ 1.3 (530 vs. 420–390). As with the single-pointing comparison above,

the superior weather at the ALMA site will increase this factor further. For example, Figure 8 shows mosaic simulations for JVLA and ALMA of a galaxy, in relatively similar compact configurations over the same 8 hours of integration. The ALMA observations are performed with fewer pointings than those of the JVLA. The resulting 1σ rms noise level of the ALMA image is a factor of three better than that of the JVLA image.

- ALMA’s larger number of baselines yield a higher “image fidelity” metric (N^3) by a factor of >6 (130000 for ALMA vs. 20000 for the JVLA) over similar observation durations. Basically, ALMA’s larger number of baselines allow more spatial frequencies to be sampled per unit time, yielding more accurate images. Figure 9 shows an example of ALMA’s higher intrinsic fidelity relative to that of the JVLA, especially for extended emission, based on simulations of a high-mass star-forming region. The difference between the model and observation images (right panel) is noticeably smaller for the ALMA case than for the JVLA one.

Table 3: Comparison of angular scale coverage between JVLA and ALMA at 45 GHz

	JVLA		ALMA	
Configuration	A	D	most extended	most compact
B_{min} (km)	0.68	0.035	0.04	0.015
B_{max} (km)	36.4	1.03	16	0.15
$\theta_{PRIMARY}$	60	60	135	135
θ_{HFBW}	0.043	1.5	0.08	9
θ_{LAS}	1.2	32	35	93

- At present, ALMA has maximum baselines that are a factor of ~ 2 smaller than the JVLA’s (15-18 km vs. 36.4 km), meaning that the JVLA can in principle produce images of resolution up to a factor of 2 higher than ALMA can at the same frequency. ALMA will be in turn more sensitive to extended emission, however. First, ALMA’s smaller dishes mean that its minimum baselines are shorter than those of the JVLA (16-m vs. 35-m; see Table 3 for a comparison), allowing higher sensitivity to extended, low-surface-brightness emission. Second, ALMA can include the ACA antennas, each of 7-m diameter but together in a close-packed configuration, in principle allowing even further sensitivity to extended emission.

In summary, ALMA Band 1 can be superior to the JVLA at its highest frequencies in many ways, including:

- **Access to southern sources**, given ALMA’s southern hemisphere location;
- **Wide-field sensitive imaging**, due to ALMA’s larger number of smaller, high precision antennas located at an excellent site;
- **High image fidelity**, given ALMA’s larger number of antennas;
- **Sensitivity to extended emission**, if appropriate, due to ALMA’s shorter minimum baselines and the ACA;
- **Likely coverage of 50-52 GHz**, frequencies not possible with the current JVLA receivers;
- **Recovery of short spacing visibilities**, by using the Atacama Compact Array, and the total power single-dish observations;
- **Combination with other ALMA bands**, for many multi-band projects; and
- **Lower overheads**, by applying for and using a single observatory.

As shown in §4, the top science cases for Band 1 can stand shoulder-to-shoulder with the primary Level 0 goals of ALMA. Thus, the primary motivation for the enhancement is *not* as a “poor weather” back-up receiver but rather the excellent science that can be achieved. In the following sections, we explore the large and broad variety of science cases beyond the top cases identified in §4 that the ALMA Band 1 receiver suite will be able to address.

6. A Broad Range of Science Cases

Along with the two science cases presented above in §4, there is a wealth of scientific opportunity available to the wide ALMA community when the Band 1 receiver suite is built. Here we highlight a selection of science cases which would significantly benefit from Band 1 receivers on ALMA.

6.1. Continuum Observations with ALMA Band 1

The astrophysical continuum radiation at wavelengths of ~ 1 cm is relatively unexplored. Yet, this radiation is key to understanding radio emission mechanisms and probing regions that are optically thick at shorter wavelengths. The sensitivity and resolution of ALMA Band 1 will allow: (1) improved understanding of galaxy clusters through the Sunyaev-Zel’dovich Effect; (2) a diagnostic of the smallest interstellar dust grains; (3) studies of jets from young stars; (4) an understanding of the nature of pulsar wind nebulae; (5) the detection of radio SNe, with constraints on stellar precursors and remnants; (6) a diagnostic of X-ray binaries; and (7) improved probes of Sgr A*, the supermassive black hole at the center of the Galaxy.

6.1.1. The Sunyaev-Zel’dovich Effect

Much of what we know about galaxy clusters has come from X-ray observations of thermal bremsstrahlung emission of the intra-cluster medium (ICM). For example, the angular resolution of *Chandra* has been crucial to advancing our understanding in this area and has resulted in a renaissance in astrophysical studies of galaxy clusters. In recent years, the Sunyaev-Zel’dovich Effect (SZE) has provided an increasingly important view of these cosmic structures (Birkinshaw 1999). Since the SZE signal is proportional to the product of the electron density and its temperature ($\sim n_e T_e$, compared to $n_e^2 \sqrt{T_e}$ for the X-rays), it gives a complementary view of the physical state of the ICM, one more sensitive to hot phases that also directly measures local departures from thermal pressure equilibrium. To date, the majority of SZE observations have been carried out at comparatively low angular resolution (beams $> 1'$ in size), yielding information about the overall bulk cluster properties. Advances in instrumentation have begun making higher angular resolution measurements of the SZE possible, revealing previously unsuspected shock-heated gas in the ICM of clusters previously thought to be dynamically relaxed (Komatsu et al. 2001, Kitayama et al. 2004, Mason et al. 2010, Korngut et al. 2011, Plagge et al. 2012). These $10''$ to $20''$ SZE images are the current state of the art. A Band 1 receiver suite on ALMA will surpass this bench-

mark, making possible detailed studies of the ICM using the SZE on larger samples and with greater sensitivity than before.

ALMA Band 1 receivers will be capable of addressing a wide range of basic questions about the observed structure and evolution of clusters. For example, what are the structures of ICM shocks and the mechanisms responsible for converting gravitational potential energy into thermal energy in the ICM (Markevitch et al. 2007, Sarazin et al. 1988)? What is the influence of Helium ion sedimentation within the cluster atmosphere (Ettori et al. 2006)? What is the nature of the AGN-inflated “bubbles” seen in the cores of some clusters (Pfrommer et al. 2005), and what is the role of cosmic rays in the ICM? What is the nature of the underlying ICM turbulence (e.g., Kolmogorov versus Kraichnan)? A particularly rich area will be the detailed study of ICM shocks, which are common since infalling sub-clusters are typically transsonic. Several galaxy cluster mergers have been observed recently with Chandra and XMM in X-rays with resolutions at the arcsecond level where substructures become visible (Markevitch, et al. 2000, 2002). The features of interest for these studies will typically fit within one or a few ALMA Band 1 fields-of-view and require longer integrations (several to ~ 10 hours per pointing). Note that Band 1 receivers also may have the sensitivity to detect the SZE from the halos of massive individual ellipticals or massive groups.

Another important area where high-resolution SZE imaging will have an impact is the interpretation of SZE survey data. ACT (Dunkley et al. 2011), SPT (Williamson et al. 2011), and *Planck* (Planck Collaboration, 2011) have all conducted 1000+ deg² surveys to detect and catalog galaxy clusters via the SZE. These surveys provide unique and valuable information about cosmology but their interpretation depends upon assumptions about the relationship between the SZE signal and the total virial mass of the halos observed. It is known that both gravitational (cluster merger) and non-gravitational processes (AGN and supernova feedback, bulk flows⁴, cosmic ray pressure) give rise to considerable scatter and potential biases (e.g., Morandi et al. 2007) in this relationship. Cluster mergers have a particularly dramatic effect on the SZE, typically generating transsonic (Mach $\sim 2-4$) shock fronts which can enhance the peak SZE in the cluster by an order of magnitude (Poole et al. 2007, Wik et al. 2008).

The systematic astrophysical uncertainties just described are the limiting factor in making cosmological inferences from the small published samples of a few dozen SZE-selected clusters (e.g., Sehgal et al. 2011). ALMA Band 1 receivers are the only foreseen prospect

⁴By bulk flow, we refer to the motion of a cluster itself through its surrounding medium, producing a kinematic contribution to the observed SZE signal; in theory, this contribution has a different spectral dependence than the thermal SZE and may be distinguishable with good spatial coverage.

for efficient high-resolution observations of the large southern hemisphere samples of SZE-selected clusters that will directly improve inferences from these surveys. They will be used to image (at $5'' - 10''$ resolution) galaxy clusters discovered in the low-resolution ($\sim 1'$) surveys, detecting shocks and mergers and identifying ICM substructure, and providing a direct, phenomenological handle on important survey systematics. Indeed, the sensitivity and resolution of an ALMA Band 1 receiver suite allows for efficient follow-up observations of cluster detections made by blind southern hemisphere SZE surveys. Thus, a study of a selection of clusters from these survey experiments in a statistical manner becomes feasible and new important insights into the mass-observable relation and its scatter and dependence on cluster physics can potentially be obtained. The ability to understand cluster selection in detail is essential to derive reliable constraints on cosmological models from SZE cluster surveys (see e.g., Geisbuesch et al. 2005; Geisbuesch & Hobson 2007).

The coming decade will also see an explosion of optical and X-ray cluster data. The German/Russian satellite *eRosita*, due to launch in 2014, will carry out the first all-sky X-ray survey since ROSAT (Merloni et al. 2012). Among other things, it is expected to catalog ~ 100000 clusters out to $z = 1.3$ (Cappellutti et al. 2011). Also, the Dark Energy Survey (DES; Dark Energy Survey Collaboration 2005) is a 5000 deg^2 , mostly southern sky survey also expected to find ~ 100000 galaxy clusters. Targeted SZE observations with ALMA Band 1 receivers will be invaluable to determine the properties of clusters at redshifts where X-ray spectroscopy and gravitational lensing begin to fail. These high- z clusters, such as the ACT-discovered SZE cluster “El Gordo” at $z = 0.89$, weighing in at $M = (2.16 \pm 0.32) \times 10^{15} \text{ M}_\odot$ (Menanteau et al. 2011), offer leverage on so-called “pink elephant” tests capable of constraining cosmological or gravitational theories based on the existence of individual extreme objects, i.e., provided their properties are accurately determined. Importantly, note that an ACA equipped with Band 1 receivers will be comparable in capability to the OVRO/BIMA arrays used in the current decade to measure the bulk SZE properties of large northern hemisphere cluster samples (Bonamente et al. 2008). Extending this capability to the southern hemisphere over the next decade is important to realize the full potential of these rich cluster samples.

Given the large number of ALMA baselines, the resulting high image fidelity and dynamic range of the data will be advantageous to SZE studies, in particular the detailed ones. In addition, long baseline data from ALMA can be used to remove accurately the intrinsic and background (i.e., gravitationally lensed) discrete source populations. These latter objects are a signal of substantial interest from another point of view, but they also set a significant “confusion noise” floor to millimeter single-dish observations, especially considering the factor of 2 – 3 boost in source confusion in clusters due to gravitational lensing (Blain et al. 2002).

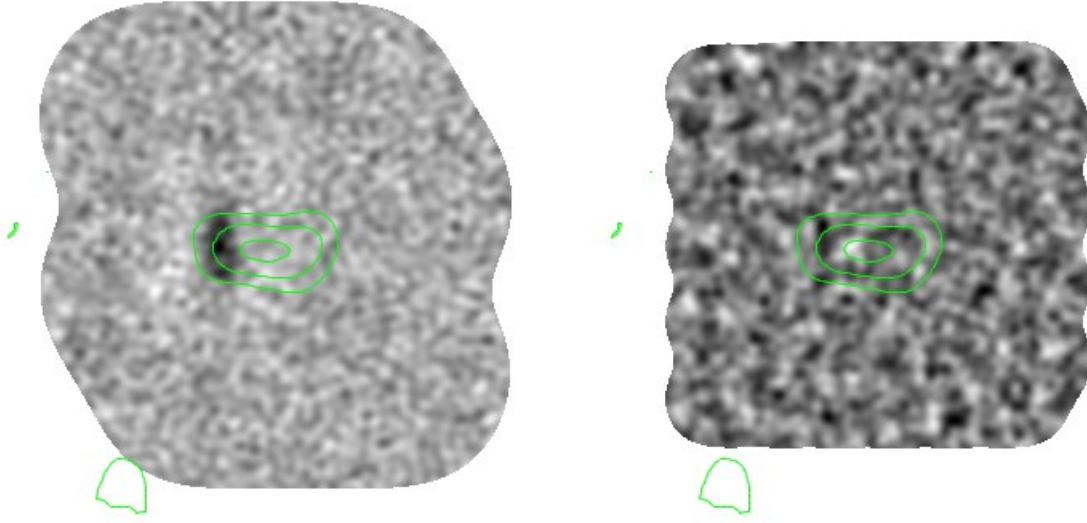


Fig. 10.— Simulated 1.5 hour ALMA Band 1 (left) and Band 3 (right) observations of a galaxy cluster covering $5' \times 5'$. The shock is represented as a Gaussian component $5'' \times 25''$ in extent with a peak SZE of $y = 10^{-4}$, considerably weaker than the amplitude observed in RXJ1347-1145 by Mason et al. (2010). The Band 3 data were tapered to the innate resolution of the Band 1 map, $\sim 10''$ (FWHM). ACA baselines were not included in this simulation but the overplotted contours show the ACA Band 1 image (using a $45''$ taper) of the bulk ICM in this system in a simulated 12 hr integration after subtraction of the shock signal. The bulk ICM is modeled as an elliptical isothermal β model with $R_{core} = (150, 250)$ kpc, $\beta = 0.7$, and $y_o = 3 \times 10^{-5}$ at $z = 0.7$, characteristic of disturbed, merging systems.

ALMA will have a considerably higher sensitivity for these observations than the JVLA, owing to an order of magnitude higher surface brightness sensitivity, or ALMA Band 3, owing to lower system temperatures and larger primary beam. In Figure 10, we show simulated Band 1 and Band 3 observations (using the ALMA 12-m Array and the ACA) that cover the virial region ($D \sim 5'$) of a moderately massive SZE cluster with a merger shock. For these simulations, we considered a hypothetical project to detect a feature with a Compton $y = 10^{-4}$, characteristic of strong shocks in major mergers, with a characteristic feature size of $5'' - 20''$. The required flux density sensitivity is similar in both cases after allowing for resolution effects, about $1\sigma = 8 - 9\mu\text{Jy}$ rms in both instances. We find that a clear detection is achieved in only 1.5 hours of Band 1 observing, but nearly 40 hours are required at Band 3. The ACA Band 1 measurement of the bulk ICM signature (a 12 hr observation is needed for good SNR) is also shown, tapered to a $45''$ FWHM beam. Yamada et al. (2012) find similar results in their detailed study of SZE imaging with ALMA and the ACA at $\lambda \approx 1\text{ cm}$.

In summary, ALMA’s southern location matching large galaxy cluster surveys, intrinsically high image fidelity, and sensitivity to extended low-brightness features (e.g., relative to the JVLA) will make Band 1 observations very compelling probes of physics of galaxy clusters using the Sunyaev-Zel’dovich Effect.

6.1.2. *Very Small Grains and Spinning Dust*

The last decade has seen the discovery of surprisingly bright cm-wavelength radio emission from a number of distinct galactic objects but most notably dark clouds (e.g., Finkbeiner et al. 2002; Casassus et al. 2008 (see Figure 11); Scaife et al. 2009). The spectrum of this new component of continuum radiation can be explained by electric dipole radiation from rapidly rotating (“spinning”) very small dust grains (VSGs), as calculated by Draine & Lazarian (1998; DL98). This emission has been also seen as a large-scale foreground in CMB maps, spatially correlated with thermal dust emission and having a spectrum peaking at $\sim 40\text{ GHz}$.

All of the existing work aimed at diagnosing this continuum emission is derived from CMB experiments on large angular scales, where the bulk of the radio signal occurs, e.g., recently by the *Planck* satellite. Details on small angular scales are crucial, however, for probing star formation and circumstellar environments. Simply, progress in the understanding of the solid and gaseous states of the ISM requires sufficient resolution to separate the distinct environments. Directly measuring the VSG abundance and solid state physics is very exciting because VSGs play a central role in the chemical and thermal balance of the ISM. For example, the smallest grains account for most of the surface area available for catalysis of molecular formation.

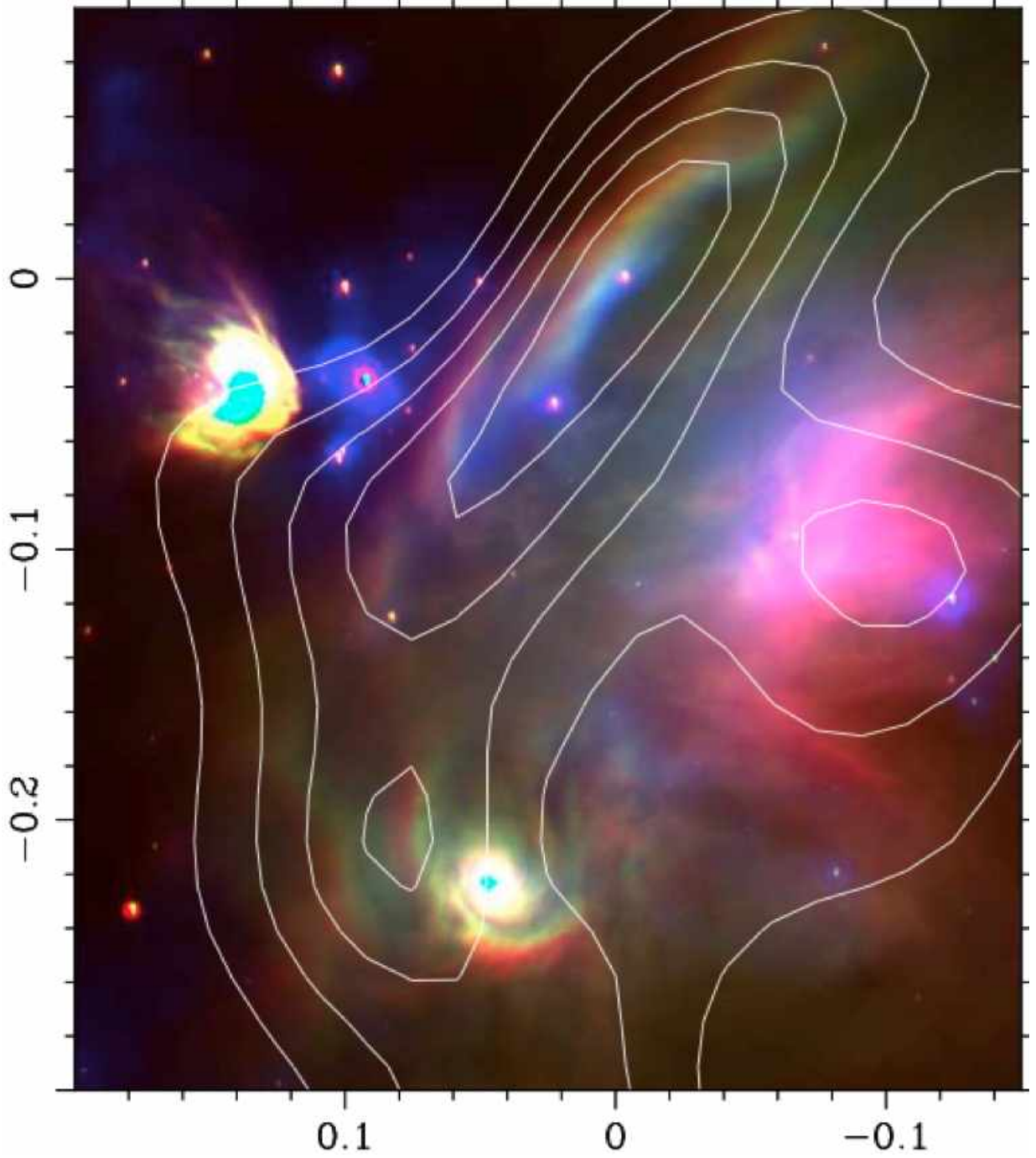


Fig. 11.— Three-colour image of the ρ Oph W photo-dissociation region (Casassus et al. 2008). **Red:** MIPS 24 μm continuum **Green:** IRAC 8 μm continuum, dominated by the 7.7 μm PAH Band **Blue:** 2MASS K_s -band image. The x - and y -axes show offset in RA and Dec from ρ Oph W, in degrees. The contours follow the 31 GHz emission, with levels at 0.067, 0.107, 0.140, 0.170, and 0.197 MJy sr $^{-1}$.

DL98 proposed that the grain size distribution in their spinning dust model would be dominated by VSGs, thought to be mostly PAH nanoparticles. The size distribution of VSGs is poorly known, however, since studies of interstellar extinction are relatively insensitive to its details. The existence of VSGs has been supported by several assertions. First, a significant amount of carbonaceous nanoparticles in the ISM could explain observations of unidentified IR emission features. Second, the strong mid-infrared emission component seen by IRAS must result from the reprocessing of starlight by ultrasmall grains. Indeed, the fraction of the ISM carbon content proposed to exist in VSGs considerably exceeds that implied to exist in the MRN dust size distribution. (The MRN dust distribution is known to underestimate this fraction.)

Observationally determining PAH content in dust clouds is not straightforward. Where there is a strong source of UV flux present, it is possible to identify PAHs by their spectral emission features. In the case of pre-stellar and Class 0 cloud cores, however, these features are absent. With observations from ALMA Band 1 receivers constraining the spinning dust SED at similar resolution to, e.g., Spitzer or the forthcoming MIRI instrument on the JWST, it will be possible to measure the VSG size distribution directly from the data.

This work will also be important in the context of circumstellar and protoplanetary disks, where the proposed population of VSGs may have important implications for disk evolution. Certainly, spinning dust emission will provide a better measure of the small grain population within circumstellar disks than PAH emission since favorable excitation conditions for PAHs exist only in the outermost layers of the disk. Since all the VSGs in the disk should contribute spinning dust emission, such emission will provide a much better probe of the mass in VSGs. Combining this information with the PAH emission features would then also give us a useful measure of sedimentation in disks.

Spinning dust emission from a VSG population will in theory dominate the thermal emission from disks (around Herbig Ae/Be stars) at frequencies ≤ 50 GHz by significant factors (Rafikov 2006). The existence of these VSGs has been confirmed observationally from PAH spectral features seen in the disks of Herbig Ae/Be stars (Acke & van den Ancker 2004) but it has not been detected in protoplanetary disks due to a lack of strong UV flux. Since spinning dust emission has been observed to be spatially correlated with PAH emission (Scaife et al. 2010), spinning dust may provide a unique window on the small grain population of these disks. In the context of disk evolution, these recent measurements conflict with the established view that dust grains are expected to grow as disks age. It may be the case that dust fragmentation is important in disks (Dullemond & Dominik 2005), or there exists a separate population of very small carbonaceous grains distinct from the MRN distribution (Leger & Puget 1984; Draine & Anderson 1985). This second proposition has not only

important implications for the study of circumstellar disks but also more generally for the complete characterization of dust and the ISM.

The arcsecond resolution necessary for these measurements will be achievable with several ALMA configurations and Band 1. From the models of Rafikov (2006), the difference between a thermal dust spectrum with $\beta \approx 1$ and the predicted spinning dust contribution for a brown dwarf disk would be observable at 5σ in a matter of minutes with ALMA Band 1 receivers. With longer observation times and consequently higher sensitivity, it will be also possible to distinguish between different grain size distributions and physical conditions within the disk (such as grain electric dipole moments, rotational kinematics, optical properties and catalysis of molecule formation).

In summary, spinning dust emission provides a unique insight into the VSG population under conditions where it is not possible to observe using mid-IR emission. The high resolution and excellent sensitivity of ALMA are ideal for differentiating the distinct environments where the VSG population resides and will be crucial for probing star formation and circumstellar regions. Specifically, Band 1 receivers will allow routine surveys of the new continuum component at its spectral maximum. The smaller minimum baselines of ALMA will make it more ideal for probing (especially at southern declinations) the more extended instances of spinning dust emission, e.g., cores, than the JVLA. Also, ALMA Band 1 observations of more compact objects like disks (see §5.1) will be better suited for comparison with those at higher frequency bands than those from the JVLA, given the more similar spatial frequency coverage afforded by observing from the same latitude.

6.1.3. *Jets from Young Stars*

Radio continuum emission is observed from the jets and winds of young stellar objects and is due to the interaction of free electrons, i.e., “free-free emission.” The radio images appear elongated and jet-like and are usually located near the base of large optical Herbig-Haro flows (Reipurth & Bally 2000). These regions usually have only sub-arcsecond sizes, indicating the youth of the emitting material and the short dynamical times involved. The emitted flux is usually weak, with a flat to positive spectral index with increasing frequency, and it can be obscured by the stronger thermal emission from dust grains at higher frequencies (e.g., Anglada 1995). Multi-wavelength studies of the brightest radio jets at centimeter wavelengths trace either earlier and stronger sources or more massive systems. The triple system L1551-IRS 5, one of the most studied low-mass systems (Rodríguez et al. 1998, 2003; Lim & Takakuwa 2006), is illustrative of the sub-arcsecond scales required (Figure 12).

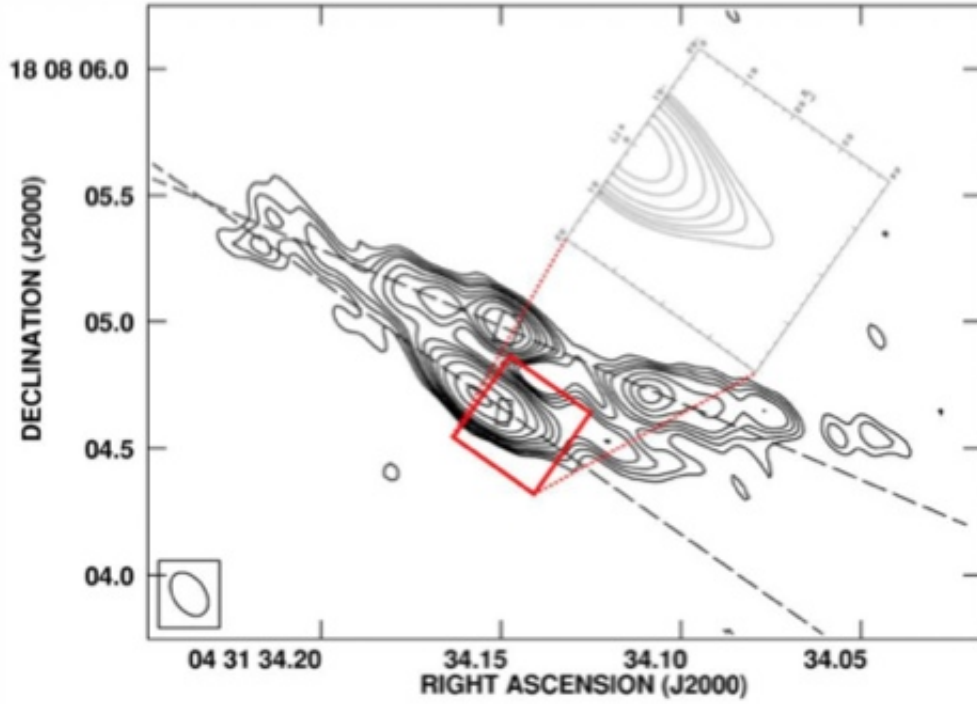


Fig. 12.— **Background:** The VLA+Pie Town continuum image of L1551 IRS 5 at 3.5 cm obtained by Rodriguez et al. (2003) in their Figure 1. The size of the beam ($0.18 \times 0.12''$; P.A. = 35°) is shown in the bottom left-hand corner. Black rectangles mark the positions and deconvolved dimensions of the 7 mm compact protoplanetary disks. The dashed lines indicate the position angles of the jet cores. **Inset:** map of the south jet from the X-Wind model convolved with the beam and plotted with the same contour levels from Figure 4 of Shang et al. (2004).

Ground-based, interferometric studies of radio jets provide the best opportunity to resolve the finest scales of the underlying source, comparable or better than optical studies of jets by HST. Such finely detailed images can provide the ability to differentiate between theoretical ideas about the nature of these jets, i.e., the launch region, the collimation process, and the structure of the inner disks. Modeling efforts with the radio continuum emission presented in Shang et al. (2004) demonstrated one such possibility in constraining theoretical parameters using earlier millimeter and centimeter interferometers (Figure 12). Band 1 observations will discriminate between competing jet launch theories tied to the disk location of the launch point by achieving better than $0.1''$ angular resolution.

The high sensitivity of ALMA Band 1 observations will also allow detection of radio emission from less luminous sources. ALMA will thus have the potential to discover a significant number of new radio jets, providing a catalog from which evolutionary changes in the physical properties can be deduced. As well, multi-epoch surveys will be able to follow the evolution of the freshly ejected material down to a few AU from the driving sources through movies. The 35-52 GHz frequency range of Band 1 will show contributions to the observed emission from both the ionized component of the jet and the thermal emission from the dust. These data, together with detailed theoretical modelling will uncover a complete understanding of properties of the spectral energy distribution (SED) from the ionized inner regions of young stellar jets.

Relative to the JVLAs, Band 1 observations with ALMA may have modest improvements in sensitivity at frequencies in common. Of course, southern sources will be much better observed with ALMA. Moreover, the wider field-of-view of ALMA will more easily allow for observations of multiple jets across crowded regions such as within young protoclusters.

6.1.4. *Spatial and Flaring Studies of Sgr A**

Near-IR and radio observations provide compelling evidence that the compact nonthermal radio source Sgr A* is identified with a $4 \times 10^6 M_{\odot}$ black hole at the center of the Galaxy (Reid and Brunthaler 2004; Ghez et al. 2008; Gillessen et al. 2009). It is puzzling, however, that the bolometric luminosity of Sgr A* due to synchrotron thermal emission from hot electrons in the magnetized accretion flow is several orders of magnitude lower than expected from the accretion of stellar winds. There have been two different approaches to address this puzzling issue. One is to search for the base of a jet from Sgr A* and identify interaction sites of a jet with the ionized and molecular material surrounding Sgr A*. The other is to study the correlations of the variable emission from Sgr A* at centimeter and millimeter bands. Studies of images and variability are well suited using ALMA's Band 1

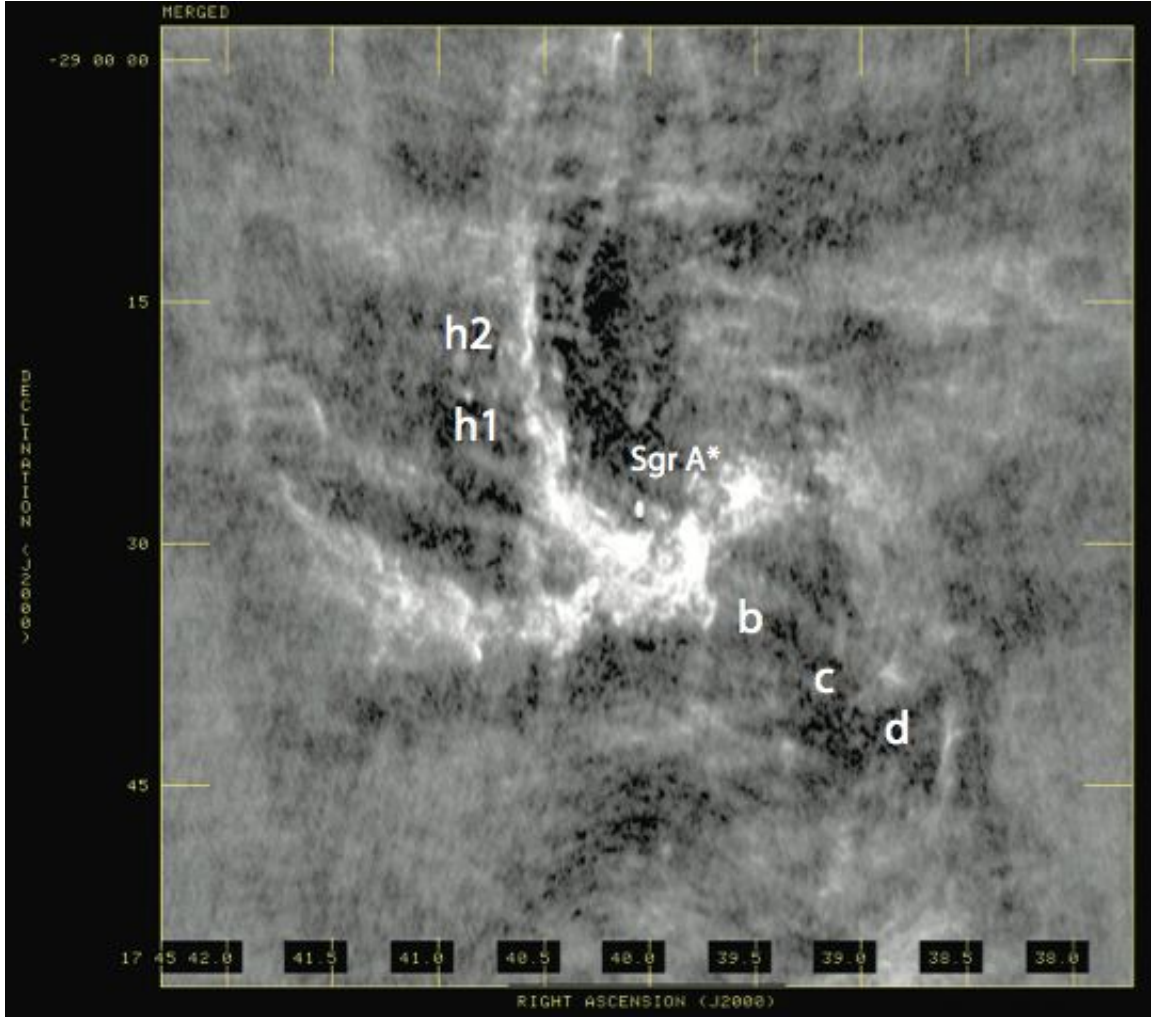


Fig. 13.— (a) Left A 22 GHz image of the Sgr A* region at $0.36'' \times 0.18''$ resolution (PA= 2°) constructed by combining JVLA A- and B- array data.

and will be complementary to each other in addressing the key question as to why Sgr A* is so underluminous. Note that Sgr A* is located at a declination of -29° , making it a more attractive target for ALMA than the JVL A.

Regarding jets, recent JVL A observations at radio wavelengths presented a tantalizing detection of a jet-like linear feature appearing to emanate from Sgr A* (Yusef-Zadeh et al. 2012). Figure 13 shows a 23 GHz image of the inner $30''$ of Sgr A*. A new linear feature is noted running diagonally crossing the bright N and W arms of the mini-spiral, along which several blobs (b, c, d, h1 and h2) are detected. What is interesting about the direction in which the linear feature is detected is that several radio blobs have X-ray and FeII/III counterparts also along the axis of the linear structure. In addition, the extension of the linear feature appears to be polarized at 8 GHz, suggesting that this feature is a synchrotron source. The radio-polarized linear jet-like structure is best characterized by a mildly relativistic jet-driven outflow from Sgr A*, and an outflow rate $\gamma\dot{M} \sim 10^{-6} M_\odot \text{ yr}^{-1}$.

The linear arrangements of antennas in the JVL A configurations can lead to linear structures in the residual beam pattern due to deconvolution errors. ALMA’s configurations, however, should lead to data with better, more-uniform uv coverage and will establish the reality of the linear structure. In particular, Band 1 will be most effective in studying the faint jet-like feature from Sgr A*. Dust emission from the immediate environment of Sgr A* dominates fluxes at shorter wavelengths relative to optically thin non-thermal emission from the jet with a steep energy spectrum. Thus, observations with Band 1 are critical for measuring properly the morphology, spectral index and polarization characteristics of the jet emanating from Sgr A*. Although Sgr A* is a unique object in the Galaxy, similar motivations also apply to other non-thermal radio continuum sources such as microquasars, e.g., 1E1740.7-2942, that have faint radio jets and are located in the inner Galaxy.

Regarding the correlations of variable emission from Sgr A*, recent radio measurements have detected a time delay of $\sim 30 \pm 10$ minutes between the peaks of 7 mm and 13 mm radio continuum emission toward Sgr A* (Yusef-Zadeh et al. 2006). This behaviour is consistent with a picture of a flare in which the synchrotron emission is initially optically thick. Flaring at a given frequency is produced through the adiabatic expansion of an initially optically thick blob of synchrotron-emitting relativistic electrons. The intensity grows as the blob expands, then peaks and declines at each frequency that the blob becomes optically thin. This peak first occurs at 43 GHz and then at 22 GHz about 30 minutes later. Theoretical light curves of flare emission, as shown in Figure 14, show that it occurs at high near-infrared frequencies first and is increasingly delayed at successively lower ALMA frequencies that are initially optically thick.

The limited time coverage of JVL A observations at radio wavelengths (due to the low

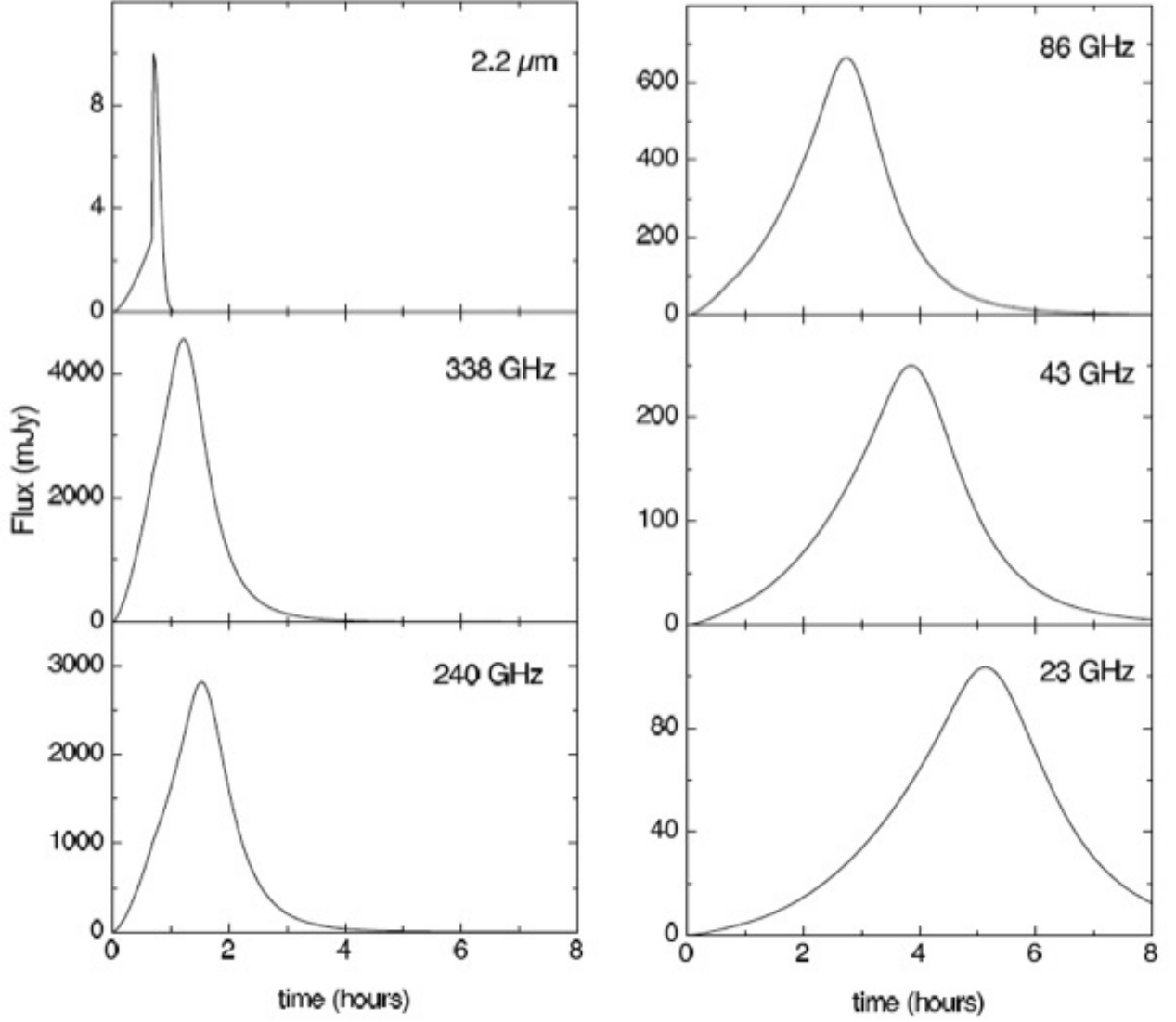


Fig. 14.— Theoretical light curves of Stokes I for optically thick synchrotron emission at five different bands corresponding ALMA Bands 3, 6, 7 and 9 as a function of expanding blob radius. These light curves assume an energy power law index $p=1$ where $n(E) \propto E^{-p}$.

maximum elevation of Sgr A* at the JVLA) means that there can be a large uncertainty in determining the underlying background flux level of a particular flare, as well as difficulty identifying flares in different bands. Observations of Sgr A* with a long time coverage using ALMA’s Band 1 can fit the corresponding light curves simultaneously to place much tighter constraints on the derived physical parameters of the flare emission region. Two parameters of high interest are the expansion speed of the hot plasma and the initial magnetic field. These quantities characterize the nature of outflow and cooling processes relevant to millimeter emission. The fitting of a light curve at one frequency will automatically generate models for any other frequency. We should be able to test the time delay between the peaks of flare emission within Band 1.

What has emerged from past observing campaigns to study Sgr A* is that radio, sub-millimeter, near-infrared, and X-ray emission can be powerful probes of the evolution of the emitting region since they are all variable. We now know that flare emission at infrared wavelengths is due to optically thin synchrotron emission that is detected when a flare is launched (Eckart et al. 2006). The relationship between radio and near-infrared/X-ray flare emission has remained unexplored due to the very limited simultaneous time coverage between radio and infrared telescopes. The continuous variations of the radio flux on hourly time scales also make the identification of radio counterparts to infrared flares difficult. In spite of the limited time coverage, the strong flaring in near-infrared/X-ray wavelengths has given us an opportunity to examine if there is a correlation with variability at radio frequencies. A key motivation for observing Sgr A* is to compare its flaring activity with the adiabatic expansion picture. One of the prediction of this model is a time delay between the peaks of optically thin near-infrared emission and optically thick radio emission, as discussed above. From this model, a near-infrared flare of short duration of 0.5-1 hr is expected to have a radio counterpart of duration of ~ 2 hr shifted in time by 3-5 hr.

Figure 15 shows composite light curves of Sgr A* obtained with XMM, VLT, HST, the IRAM 30-m Telescope, and the VLA on 2007 April 4. These curves reveal that there was no significant variation at 240 GHz during the period when the strong near-infrared/X-ray flare took place. The IRAM observation shows an average flux of $3.42 \text{ Jy} \pm 0.26 \text{ Jy}$ between 5 hr and 6h UT when the powerful near-infrared flare took place. The millimeter flux is mainly arising from the quiescent component of Sgr A*. Comparing the light curves of the 43 GHz and 240 GHz data, there is no evidence for a simultaneous radio counterpart to the near-infrared/X-ray flare with no time delays. Given the limited coverage in time with the VLA, it is clear that we can not be confident about the time delay between radio and near-infrared/X-ray peaks. There is also no overlap in time between the VLA and Subaru data to test the adiabatic picture of flare emission by making simultaneous NIR and radio observations. In future, ALMA and VLT will have the best time overlap to test this

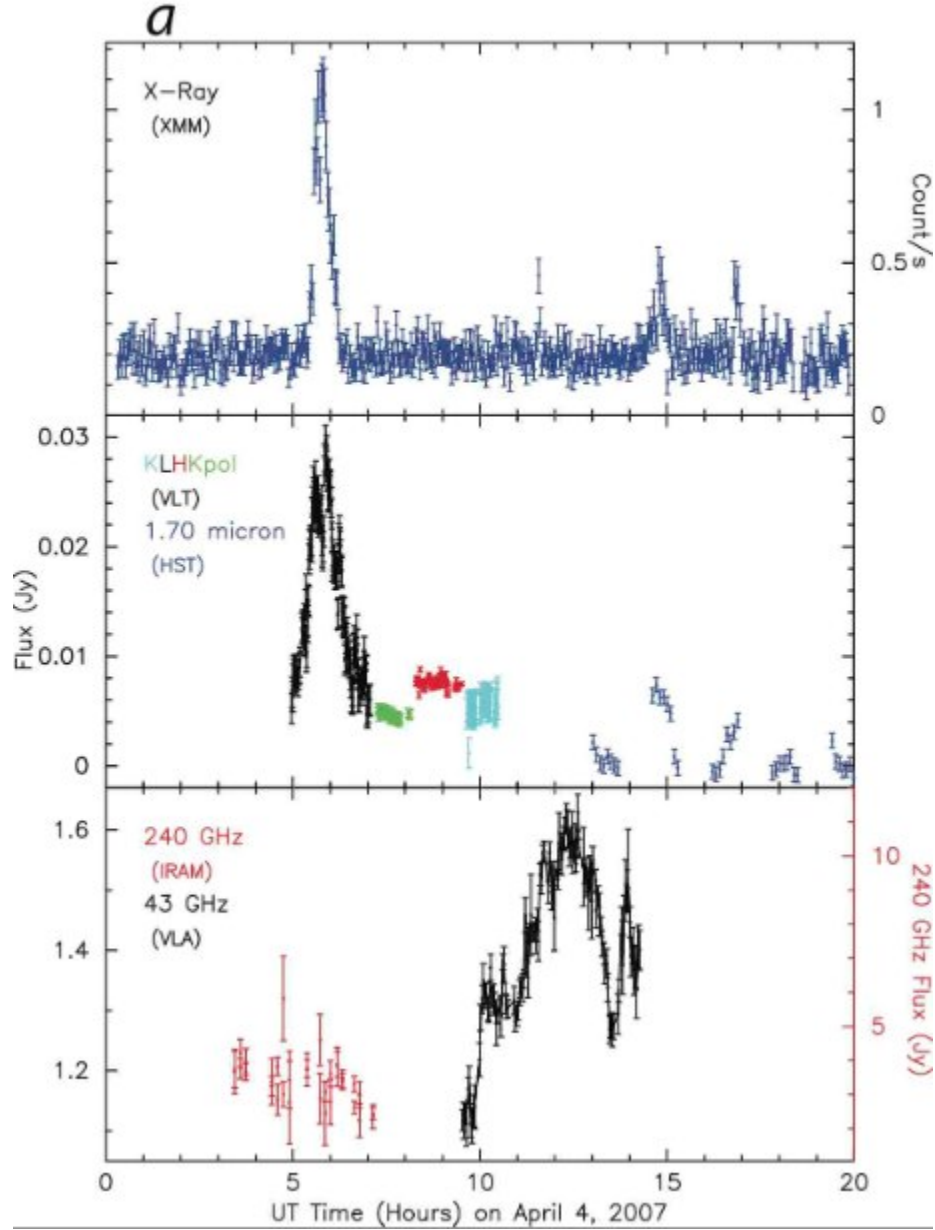


Fig. 15.— The light curves of Sgr A* on 2007 April 4 obtained with XMM in X-rays (top), VLT and HST in NIR (middle), and IRAM-30m and VLA at 240 GHz and 43 GHz, respectively (bottom). The NIR light curves in the middle panel are represented as H ($1.66 \mu\text{m}$) in red, K_s and K_s -polarization mode ($2.12 \mu\text{m}$) in green and light blue, respectively, L' ($3.8 \mu\text{m}$) in black (Dodds-Eden et al. 2009), and NICMOS of HST in blue at $1.70 \mu\text{m}$. In the bottom panel, red and black colors represent the 240 GHz and 43 GHz light curves, respectively.

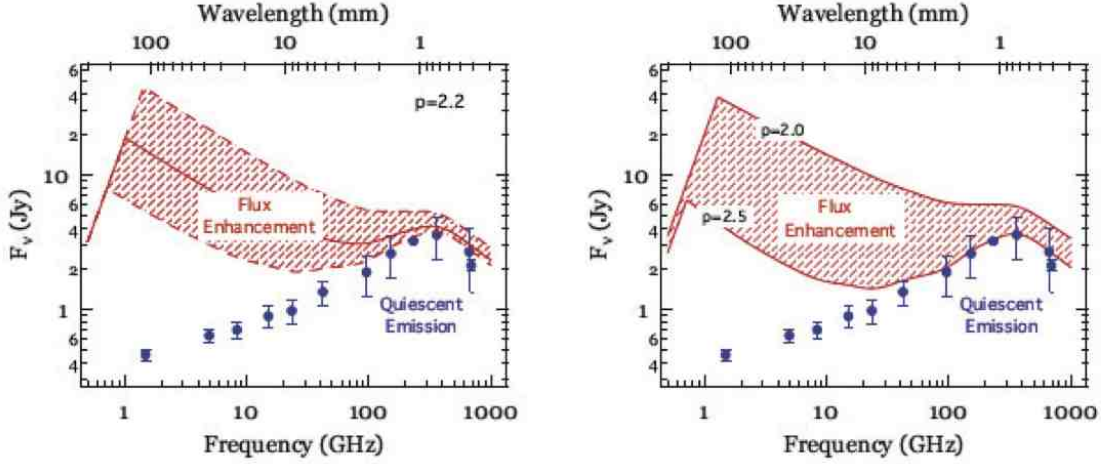


Fig. 16.— Radio emission as a function of frequency expected from G2 cloud (red) when compared to quiescent emission from Sgr A*, as shown in blue (Narayan, Ozel, & Sironi 2012). Left and right panels show predictions based on different assumptions on the energy spectrum of nonthermal particles (p).

important aspect of flare emission from Sgr A*. Although Sgr A* is a unique object in the Galaxy, similar arguments could be made for numerous transient sources found in the inner Galaxy.

Finally, we note the utility of ALMA Band 1 receivers to trace close encounters of gas clouds with Sgr A*. For example, a $3 M_{\text{Earth}}$ cloud of ionized gas and dust named G2 has been recently determined to be on a collision course with Sgr A*. VLT observations indicate that the G2 cloud approaches pericenter in mid-2013 and it will be disrupted and portions will likely be accreted by the massive black hole residing there (Gillessen et al. 2012). At the pericenter distance, the velocity of the gas cloud will be 5400 km s^{-1} . Accordingly, the cloud is expected to produce a bow shock that can easily accelerate electrons into a power-law distribution of index $p = 2.5 - 3.5$, assuming standard shock conditions (Narayan et al. 2012). Depending on p , the expected additional emission from Sgr A* ranges from 0.6 Jy to 4 Jy, over a dynamical timescale of ~ 6 months. The model behind the additional radio emission from the disruption of G2 by the black hole could have been tested directly with ALMA Band 1 observations. Though Band 1 receivers will not be ready for the interaction of G2 with Sgr A* by 2013, this close encounter is likely not an isolated event, and future disruptions of other, similar clouds in the Sgr A* region by the black hole could be monitored with Band 1.

In summary, ALMA Band 1 receivers will provide important constraints to models of Sgr A*, the supermassive black hole in the center of the Galaxy. ALMA’s southern location will allow for improved observations of Sgr A* than possible at the JVLA site, due to the southern declination of the object. For example, the longer time Sgr A* is present over the horizon improves studies of variability, and also improves sensitivity and spatial frequency coverage for observations of associated phenomena at Band 1 frequencies.

6.1.5. *Acceleration Sites in Solar Flares*

When a solar flare occurs, some of the particles in the corona are accelerated from a few hundred eV up to a few MeV within less than one second. The non-thermal electrons accelerated by a flare flow along the magnetic field lines of the flare, emitting microwaves while propagating through the corona. Finally, they collide with the dense and cool plasma in the chromosphere and lose the energy by radiation and thermalization. In most flares, two hard X-Ray (HXR) sources are observed at the footpoints of the flare loop, and one microwave source is observed around the top of the loop (see Figure 17). Previous observations of these sources had been done by HXR and microwave solar telescopes with low spatial resolution (e.g., ~ 10 arcsec) and low dynamic range (10–100). Hence, it has been hard to investigate the structures and time evolution of the sources behind particle acceleration, especially since we do not yet know where the acceleration site is in a flare. Some indirect evidence suggests that the acceleration site is located above the flare loop, in a location filled with ~ 10 MK thermal plasma (Masuda et al. 1994, Aschwanden et al. 1996, Sui and Holman 2003), but there is no direct evidence yet. Currently, it is also impossible to investigate the relationship of the acceleration site with the thermal structures, like the in-flow of magnetic reconnection detected by the EUV observations (Yokoyama et al. 2001). Therefore, there has been no significant progress in the study of the particle acceleration in the last decade.

Breakthroughs in the study of the particle acceleration in a solar flare may be possible by solar ALMA observations even with ALMA’s current specs, because its spatial resolutions and dynamic ranges are one order magnitude higher than the current solar HXR and microwave telescopes. Nevertheless, the possibility is very tiny for two important reasons: 1) the field-of-view of ALMA Band 3, the presently lowest observing frequency receiver of ALMA, is about $60''$. That field-of-view is not large enough for most flare observations and also it would be very hard to observe simultaneously the region above the flare loop predicted to be the acceleration site and the flare loop itself. Moreover, the size of the field-of-view is directly related to the possibility of observing flares, since the duration of solar observations by ALMA is limited. 2) If the acceleration site is above the flare loop, as suggested by indi-

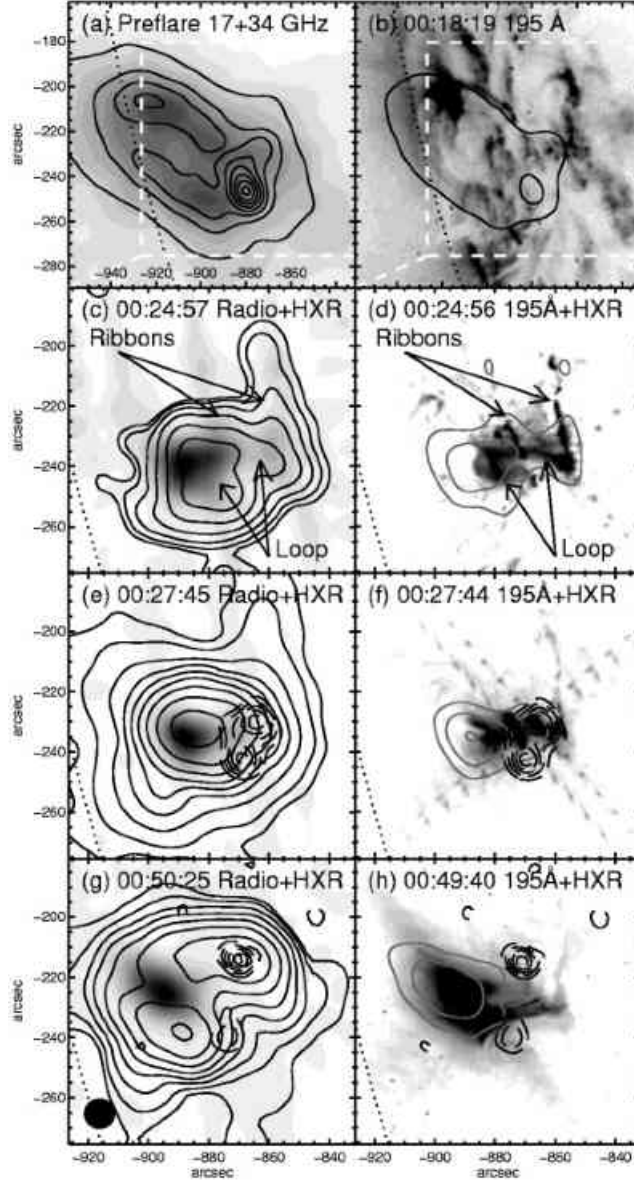


Fig. 17.— Images of a solar flare at X-ray, EUV, and radio wavelengths. The top row panels show radio and EUV images in the pre-flare phase. On the left are 17 GHz contours overlaid on a greyscale 34 GHz image (both averaged over the period 23:00–00:15 UT), while the right panel shows a 195 Å image from 00:18:19 UT together with two 17 GHz contours for context. The remaining rows of panels show the $96'' \times 96''$ region outlined in the pre-flare images. The left panels show the RHESSI greyscale image of 12–20 keV HXR overlaid with 17 GHz total intensity radio contours (solid curves) and RHESSI 100–150 keV HXR contours (dashed curves). The right panels show a 195 Å image of the same region overlaid with solid grey contours for the RHESSI 12–20 keV HXR and dashed black contours for the RHESSI 100–150 keV HXR. The panel labels refer to the times of the 17 GHz images (left) and the TRACE images (right). Figure from White et al. (2003).

rect evidence, we can easily infer that the magnetic field strengths at the site is a few tens of Gauss. The emissivity of the microwaves emitted by the gyro-synchrotron mechanism, however, strongly depends on the magnetic field strength. Therefore, emission at frequencies of 230 GHz and higher from the acceleration site is very weak. Such high frequency emission has been detected only from the main sources of large flares by submillimeter single-dish observations (e.g., Kaufmann, et al. 2004). Therefore, a lower frequency band with the high spatial resolution and dynamic range of ALMA is needed to observe the non-thermal emission from the acceleration site. Flare observations with ALMA Band 1, with a single-pointing field-of-view of about $100''$ in the 35–50 GHz frequency range, will obtain significantly better results for the particle acceleration studies of a solar flare. If the Band 1 receiver has also the capability to observe circular polarization, even higher scientific returns will be achieved, because the circular polarization of the gyro-synchrotron emission will reveal the magnetic field strength of the emitting region.

The JVLA can also observe the Sun at similar frequencies as those of Band 1, but JVLA solar observations have several disadvantages. First, the JVLA has a more reduced u – v coverage. To synthesize a solar image, snapshot data are needed because the non-thermal emission from a solar flare changes within less than one second. Hence, ALMA’s larger number of baselines means that a larger number of data points will be instantaneously sampled on the u – v plane. Second, since the JVLA antennas are larger than the ALMA antennas and the JVLA cannot sample as many short spacings, the maximum angular scale observable with the JVLA is $\sim 32''$, making it harder to reconstruct flare loops than with ALMA. Finally, the field-of-view of the JVLA, $\sim 60''$, is relatively small.

The total flux of gyro-synchrotron emission emitted from a solar flare follows a power-law distribution with frequency in the optically-thin frequency range, so lower frequency observations are more sensitive in detecting flares. The typical turnover frequency of flares is about 10 GHz. Therefore, the total flux of emission in the Band 1 frequency range is one to two orders of magnitude larger than that in Band 3. Nobeyama polarimeter data have shown that the total flux average from 700 solar flares at 35 GHz is 46.3 SFU (4.63×10^5 Jy). Special care has to be taken to deal with such a large input flux.

6.1.6. *Pulsar Wind Nebulae*

Pulsars generate magnetized particle winds that inflate an expanding bubble called a pulsar wind nebula (PWN) whose outer edge is confined by the slowly expanding supernova ejecta. Electrons and positrons are accelerated at the termination shock some 0.1 pc distant from the pulsar. Those relativistic particles interact with the magnetic field inside the wind-

blown bubble to produce synchrotron emission across the entire electromagnetic spectrum. Particles accelerated at the shock form toroidal structures, known as wisps, and some of them are collimated along the rotation axis of the pulsar, contributing to the formation of jet-like features. The synchrotron emission structure in the post-shock and jet regions provide direct insight on the particle acceleration process, magnetic collimation, and the magnetization properties of the winds in PWNe. These observations have so far (except for the Crab Nebula) been limited to X-ray wavelengths with the *Chandra* satellite (e.g., Helfand et al. 2001).

ALMA has the sensitivity and resolution necessary to detect PWNe features at high radio frequencies, where we can detect the emission from relativistic particles that have much longer lifetimes than in X-rays. At cm/mm-wavelengths, flat-spectrum synchrotron PWNe stand out over steep-spectrum SNRs (e.g., as seen in the Vela PWN (Hales et al. 2004), discussed in § 6.1.6 below, and illustrated in Figure 18 (Bietenholz et al. 2004)) with minimal confusion from the Rayleigh-Jeans tail of submm dust. ALMA Band 1 receivers will allow observations in the frequency regime where PWNe dominate, and bridge an important gap in frequency coverage, where spectral features such as power-law breaks occur and linear polarization observations do not suffer from significant Faraday rotation. Here, even the modest improvements in sensitivity of ALMA in Band 1 over the JVLA at similar frequencies will be important. Also, of course, southern PWNe will be much better probed with ALMA.

6.1.7. *Radio Supernovae*

Radio supernovae occur when the blast wave of a core-collapse supernova (SN) sweeps through the slowly expanding wind left over from the progenitor red supergiant. Particle acceleration and magnetic field amplification lead to synchrotron radiation in a shell bounded by the forward and reverse shocks (Chevalier 1982). In general, free-free absorption of the radiation in the ionized foreground medium coupled with the expansion of the SN causes the radio light curve first to rise at high frequencies and subsequently at progressively lower frequencies while the optical depth decreases. When the optical depth has reached approximately unity, the radio light curve peaks and decreases thereafter (e.g., Weiler et al. 2002). These characteristics allow estimates to be made of the density profiles of the expanding ejecta and the circumstellar medium and also of the mass loss of the progenitor. Resolved images of SNe provide information, e.g., on the structure of the shell, size, expansion velocity, age, deceleration, and magnetic field, in addition to refined estimates of the density profiles and the mass loss (Bartel et al. 2002). Radio observations of SNe can be regarded as a time

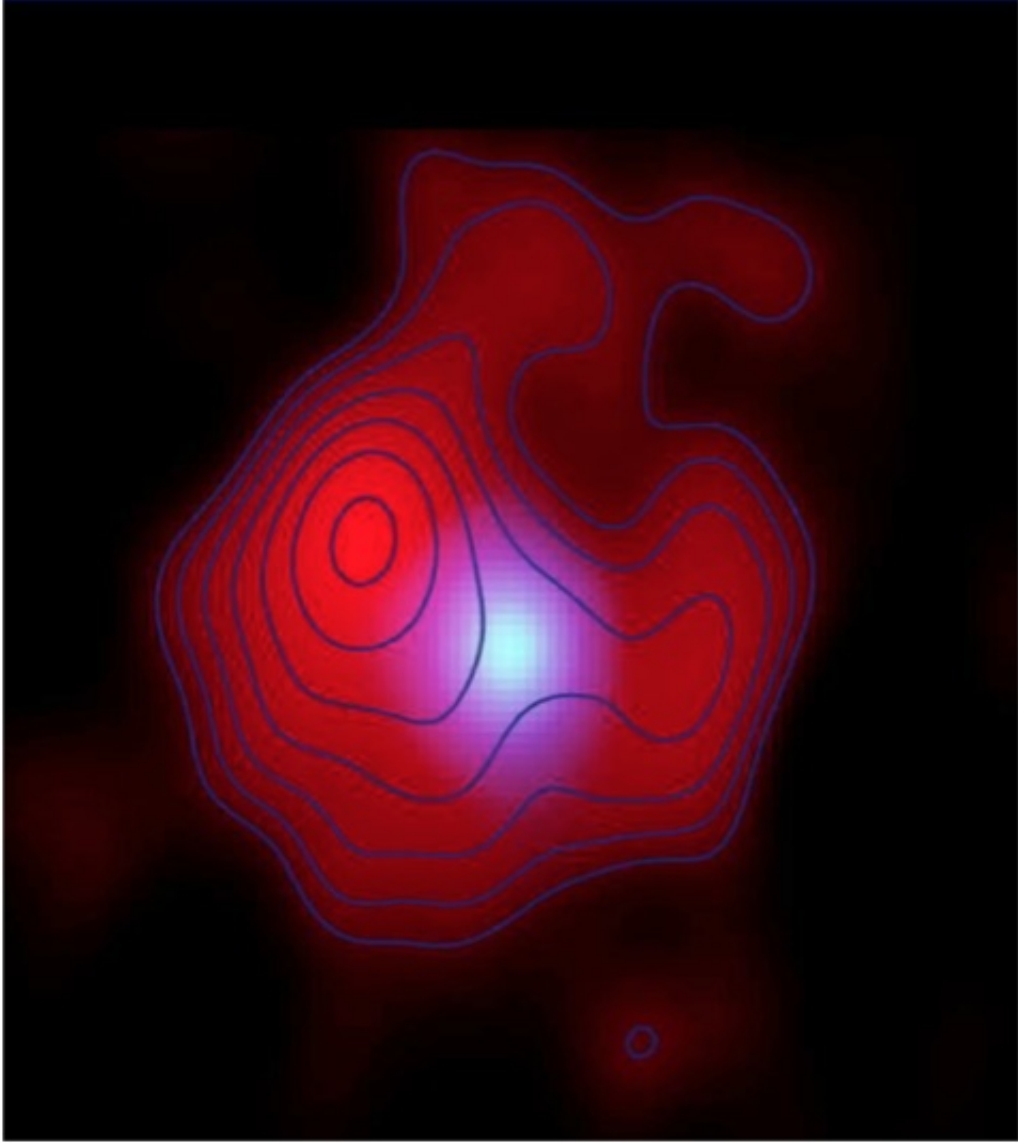


Fig. 18.— Two-colour VLBI image of SN 1986J highlighting the emergence of a central component. The red colour and the contours represent the 5.0 GHz radio brightness. The contours are drawn at 11.3, 16, 22.690.5% of the peak brightness of 0.55 mJy/bm. The blue to white colours show the 15 GHz brightness of the compact, central component. The scale is given by the width of the picture of 9 mas. North is up and east to the left. For more information on the emergence of the compact source, see Bietenholz et al. (2004).

machine, where the history of the mass loss of the progenitor is recorded tens of thousands of years before the star died. Finally, the SN images can be used to make a movie of the expanding shell of radio emission and to obtain a geometric estimate of the distance to the host galaxy (Bartel et al. 2007).

ALMA Band 1 receivers will allow exciting science to be done in the areas of radio light curve measurements, imaging of a nearby SN and, in conjunction with VLBI, imaging of more distant SNe. Depending on the medium, the delay between the peak of the radio light curve at 20 cm and 1 cm can be as long as 10 years, as for instance was the case of SN 1996cr (Bauer et al. 2008). Absorption can also occur in the source itself. In case of SN 1986J, a new component appeared in the radio spectrum and in the VLBI images about 20 years after the explosion and then only at or around 1 cm wavelength. The component is located in the projected center of the shell-like structure of the SN and may be emission from a very dense clump fortuitously close to that center, or possibly from a pulsar wind nebula in the physical center of the shell (Figure 18, Bietenholz et al. 2004, 2010). Observations in Band 1 minimize the absorption effect relative to observations at longer wavelengths and thus allow investigations of SNe at the earliest times without compromising too much on the signal to noise ratio of a source with a steep spectrum. ALMA with Band 1 receivers has the sensitivity to measure the radio light curves of 10s to 100 SNe. In addition, ALMA may be then also particularly sensitive in finding “SN factories” in starburst galaxies (e.g., Lonsdale et al. 2006) where relatively large opacities would otherwise hinder or prevent discovery.

ALMA with Band 1 receivers will allow high-dynamic range images of SN 1987A in the Large Magellanic Cloud with a resolution of about 300 FWHM beams across the area of the shell in 2014. Such data would be a significant improvement over presently obtainable images (Gaensler et al. 2007; Lakićević et al. 2012). Also, since the size of the SN increases by one Band 1 FWHM beam width per 3 years, the expansion of the shell can be monitored accurately and in detail, making this SN an important target for ALMA.

In summary, ALMA Band 1 receivers could make strides in observing high-frequency synchrotron from supernovae, allowing important measurements of their properties. ALMA’s location in the southern hemisphere makes investigations of southern SNe (especially SN 1987A) especially compelling. Note that ALMA’s southern berth also would make it an important element of VLBI arrays operating in Band 1, providing southern baselines and high sensitivity. Previous SN VLBI observations at 1 cm wavelength have provided clues about physical conditions at the earliest times after the transition from opaqueness to transparency, and SN VLBI with Band 1 will surely focus on this area of research.

6.1.8. *X-ray Binaries*

X-ray binaries (i.e., binary star systems with either a neutron star or a black hole accreting from a close companion) frequently show jet emission. Most of these systems are transients. Typically, 1-2 black hole X-ray binaries undergo a transient outburst per year, while neutron stars outburst at a slightly higher rate. Outbursts typically last several months (although there are some which are both considerably longer or shorter), and during outbursts, X-ray luminosities can change by as much as 7 orders of magnitude. The radio luminosities of systems seen to date correlate well with the hard X-ray luminosities (i.e., those above ~ 20 keV), albeit with considerable, yet poorly understood scatter.

When the X-ray spectra become dominated by thermal X-ray emission, the radio emission often turns off (e.g., Tananbaum et al. 1972; Fender et al. 1999), but the extent to which the flux turns down is still poorly constrained. This turndown is not seen in neutron star X-ray binaries (Migliari et al. 2004). The reduced radio emission in black hole X-ray binaries when they have soft X-ray spectra can be explained by models of jet production in which the jet power scales with the poloidal component of the magnetic field of the accretion flow (e.g., Livio, Ogilvie & Pringle 1999), and may have implications for the radio loud/quiet quasar dichotomy (e.g., Meier 1999; Maccarone, Gallo & Fender 2003). The still-present radio emission from neutron stars in their soft state may be indicating that the neutron star boundary layers play an important role in powering jets (Maccarone 2008). The soft states of X-ray transients are short-lived. During them, there may be decaying emission from transient radio flares launched during the state transitions. Therefore, to place better upper limits on the radio jets produced during the soft state, a high sensitivity, high frequency system with a very high duty cycle is needed.

The radio properties of X-ray binaries with neutron star primaries are much more poorly understood than those of black hole X-ray binaries. This situation is partially because the neutron star X-ray binaries are fainter in X-rays than are the black hole X-ray binaries. There is, however, additionally some evidence that neutron star X-ray binaries show a steeper relation between X-ray luminosity and radio luminosity than do the black hole X-ray binaries, with $L_R \propto L_X^{0.7}$ for the black holes and $L_R \propto L_X^{1.4}$ for the neutron stars. This difference may be explained if the neutron stars are radiatively efficient (i.e., with the X-ray luminosity scaling with the accretion rate) while the black holes are not (i.e., with the X-ray luminosity scaling with the square of the accretion rate, as has been proposed by Narayan & Yi 1994) – see Koerding et al. (2006). Radio/X-ray correlations for neutron star X-ray binaries are, to date, based on small numbers of data points from few sources, and the most recent work (Tudose et al. 2009) indicates that the situation may be far more complex than the picture presented above.

In summary, Band 1 frequencies are important for resolving the relationship between radio and X-ray flares in transient events from neutron star and black hole binaries. ALMA with Band 1 receivers would provide the ability to catch such events at southern declinations. ALMA’s high sensitivity is especially important to constrain the downturns at radio wavelengths seen in many events.

6.2. Line Observations with ALMA Band 1

As with the continuum science cases, numerous examples of scientific opportunity will be available to ALMA users interested in the numerous lines located in the Band 1 frequency range from molecular rotational transitions and radio recombination lines. Here we discuss some science cases that involve high sensitivity observations of lines, including studies of (1) chemical differentiation in cloud cores; (2) the chemistry of complex carbon-chain molecules; (3) ionized gas in the dusty nuclei of starburst galaxies; (4) the photoevaporation of protoplanetary disks; (5) inflows and outflows from HII regions; (6) masers; (7) magnetic field strengths in dense gas; (8) molecular outflows from young stars; (9) the co-evolution of star formation and active galactic nuclei; and (10) the molecular gas content of star-forming galaxies at $z \sim 2$.

6.2.1. *Fine Structure of Chemical Differentiation in Cloud Cores*

Previous single-dish millimeter molecular line observations have found that molecular abundance distributions differ significantly between individual dark cloud cores. A widely accepted interpretation of this chemical differentiation is that there exists non-equilibrium gas-phase chemical evolution through ion-molecule reactions within dark cloud cores. Younger cores are rich in “early-type” carbon-chain molecules such as CCS and HC₃N, while more evolved cores, closer to protostellar formation via gravitational collapse, are rich in “late-type” molecules such as NH₃ and SO (Suzuki et al. 1992). Recent high-resolution millimeter-line observations, however, have revealed that there are even finer variations of molecular distributions within cores down to ~ 3000 AU scales, and that these fine-scale chemical fluctuations cannot be explained by the simple scenario of chemical evolution of cores (Takakuwa et al. 2003, Buckle et al. 2006). The explanation suggested for this behaviour is that there is first molecular depletion onto grain surfaces in these regions and then subsequent reaction and desorption of molecules back to the gas phase through clump-to-clump collisions or energy injection from newly formed protostars (e.g., Buckle et al. 2006). The molecules that can differentiate between regions with “early-type” chemistry, before any collapse of a

protostellar object, and the “late-type” chemistry, apparent after the formation of a protostellar core, have their ground-state (strongest) transitions in ALMA Band 1. These heavy saturated organic molecules can only be formed on the surfaces of dust grains, and so their appearance in the interstellar medium signals the presence of a central heating source, likely a protostar. ALMA Band 1 receivers will provide the most sensitive test of when a central heating source turns on, since ALMA will then have the resolution and sensitivity to detect the presence of these complex molecules within a dense core of more diffuse, unprocessed gas.

Other recent work (see Garrod, Weaver & Herbst 2008 and references therein) has shown some surprising detections of saturated complex organic molecules around apparently quiescent dust cores, consistent with model predictions for the “warm-up” chemistry expected when a core is undergoing gravitational collapse and forming an internal heating source. According to models, a later stage in this sequence occurs when complex saturated molecules produced on grain surfaces react as the gas warms up, producing “hot core” chemistry, with even more complex products.

In summary, ALMA Band 1 receivers will allow probes of the smallest length scales of chemical variation in cloud cores to clarify the relationship among different molecular abundance distributions (in conjunction with chemical models). These projects will require both ALMA’s excellent spatial resolution and in particular its ability to recover the larger-scale structure of cores through observations with the ACA. Indeed, ALMA’s higher sensitivity to extended, surface brightness emission and high fidelity make observations of such lines preferable to observations of them with the JVL. Also, ALMA Band 1 will likely include 50-52 GHz, a frequency range unavailable with the JVL that contains many interesting lines, including C_3H_2 $1_{1,1}-0_{0,0}$ at 51.8 GHz. Table 4 lists some molecular transitions needed for the chemical studies within these clouds that are observable over 35-52 GHz.

6.2.2. *Complex Carbon Chain Molecules*

Band 1 receivers will provide the opportunity to search with ALMA for new complex organic molecules, including the amino acids and sugars from which life on Earth may have originally evolved. In addition, these complex molecules provide a powerful tool for understanding star formation and the processes surrounding it.

There are several reasons why Band 1 is the best place to search for complex molecules. First, the heavier a molecule, the lower will be its rotational transition frequencies. The many abundant lighter molecules (e.g., CO, HCN, CN) have their lowest transitions in Band 3, and

Table 4: Molecular Transitions between 35 GHz and 52 GHz

SO	2_3-2_2	36.202040 GHz
HC ₃ N	4–3	36.392332 GHz
HCS ⁺	1–0	42.674205 GHz
SiO	1–0	43.42376 GHz
HC ₅ N	17–16	45.264721 GHz
CCS	4_3-3_2	45.379033 GHz
HC ₃ N	5–4	45.490316 GHz
CCCS	8–7	46.245621 GHz
C ₃ H ₂	$2_{1,1}-2_{0,2}$	46.755621 GHz
C ³⁴ S	1–0	48.206956 GHz
CH ₃ OH	1_0-0_0	48.372467 GHz
CS	1–0	48.99096 GHz
HDO	$3_{2,1}-3_{2,2}$	50.23630 GHz
HC ₅ N	19–18	50.58982 GHz
DC ₃ N	6–5	50.65860 GHz
O ₂	N=35-35, J=35-34	50.98773 GHz
CH ₃ CHO	1(1,1)-0(0,0)	51.37391 GHz
NH ₂ D	1(1,0)–1(1,1)	51.47845 GHz
CH ₂ CHCHO	$1_{11}-0_{00}$	51.59607 GHz
C ₃ H ₂	$1_{1,1}-0_{0,0}$	51.841418 GHz

so do not appear at all in Band 1. Therefore, Band 1 does not suffer from contamination from these common molecules, and so line confusion is much less of a problem. Second, system temperatures at Band 1 frequencies will be significantly lower than in higher bands, giving extra sensitivity to detect weak transitions from less abundant complex molecules, such as glycolaldehyde, the simple sugar known to exist in the interstellar medium. Table 5 lists some complex carbon-chain molecules whose transitions have been already detected in the ISM. Note that searches for complex molecules can be made with Band 1 also using lines in absorption against bright background objects like, e.g., young stars or quasars.

There is now a significant body of evidence to suggest that complex biological molecules, such as amino acids and sugars needed for evolution of life on Earth, evolved in the interstellar medium (e.g., see Holtom et al. 2005; Hunt-Cunningham & Jones 2004; Bailey et al. 1998). Band 1 receivers will be one of the best instruments in the world to test this hypothesis observationally.

As with the molecular transitions described in §6.2.1, ALMA’s sensitivity to low surface brightness line emission through the smaller minimum baselines of the 12-m Array and the ACA itself makes exploring complex carbon-chain molecular chemistry preferable with ALMA than the JVL A over 35-50 GHz. In addition, the likely addition of 50-52 GHz to the Band 1 frequency range is not available at the JVL A.

Table 5: Some detected ISM complex carbon chain molecules

CH ₂ CHCN	propenitrile
CH ₂ CNH	ketenimine
CH ₃ C ₄ H	methyldiacetylene
CH ₃ CCCN	methyl cyanoacetylene
CH ₃ CH ₂ CN	ethyl cyanide
CH ₃ CHO	acetaldehyde
CH ₃ CONH ₂	acetamide
CH ₃ OCH ₃	ethyl butyl ether
CH ₃ OCHO	methyl formate
C ₆ H [−]	hexatriyne anion
C ₈ H	octatetraynyl
H ₂ CCCC	cumulene carbene
HCCCNH ⁺	...

6.2.3. Radio Recombination Lines

In the radio and submillimeter, we have access to an extinction-free ionized gas tracer: radio recombination lines (RRLs). These lines can measure the density, filling factor, temperature, and kinematics of the ionized gas in young star-forming regions that are still heavily obscured by dust. Measuring the properties of the ionized gas in these regions allows us to probe the properties of the interstellar medium and the stars in a very early stage of star formation. RRLs in the ALMA Band 1 frequency range (e.g., H53 α at 43.309 GHz) trace ionized gas with densities of 10⁴ cm^{−3}, which is similar to the densities of young HII regions (Churchwell 2002).

Using RRLs detected in ALMA Band 1, we can:

- measure the properties of the ionized gas and young massive stars in the dusty nuclei of starburst galaxies (see Figure 19; Kepley et al. 2011),

- detect the photoevaporation of protoplanetary disks (Pascucci, Gorti & Hollenbach 2012), and
- quantify the properties of inflows and outflows from HII regions (Peters et al. 2012) and possibly gas ionized by jets from young stars (Shepherd et al. 2013).

In the past, RRLs were difficult to observe – particularly in external galaxies – because they are faint and broad lines. Today, the high sensitivity and wide bandwidths of facilities like ALMA make RRLs more accessible. The wide band widths also allow us to stack RRLs. RRL properties change slowly with frequency, so stacking all RRLs observed within a band improves the sensitivity of the observations without increasing the observing time or affecting the properties of the line.

RRLs are brighter at higher frequencies, but they also are further apart in frequency space. ALMA Band 1 frequencies are ideal for RRL detection because the lines are bright and we can detect 3-4 lines in the 8 GHz of bandwidth provided by the ALMA correlator. At lower frequencies, the lines will be fainter; at higher frequencies, we cannot stack as many lines.

Modeling RRL emission requires a sensitive measurement of the free-free continuum. At the ALMA Band 1 frequencies, the free-free continuum begins to dominate over the synchrotron and dust continua, making measuring the free-free component straightforward. Modeling RRLs at frequencies higher than ~ 100 GHz requires disentangling free-free and dust emission.

In summary, ALMA Band 1 receivers will allow the RRLs in its frequency range to be observed towards many possible targets, including the dusty nuclei of starburst galaxies, photoevaporating disks, and HII regions. The southern location of ALMA will allow southern examples of these sources to be easily observed to high sensitivity.

6.2.4. *Maser Science*

Masers (Microwave Amplifications by Stimulated Emission of Radiation) frequently occur in regions of active star formation, from molecular transitions whose populations are either radiatively or collisionally inverted. A photon emitted from this material will interact with other excited molecules along its path, stimulating further emission of identical photons. This process leads to the creation of a highly directional beam that has sufficient intensity to be detected at very large distances.

Masers are observed from a variety of molecular and atomic species and each serves as a

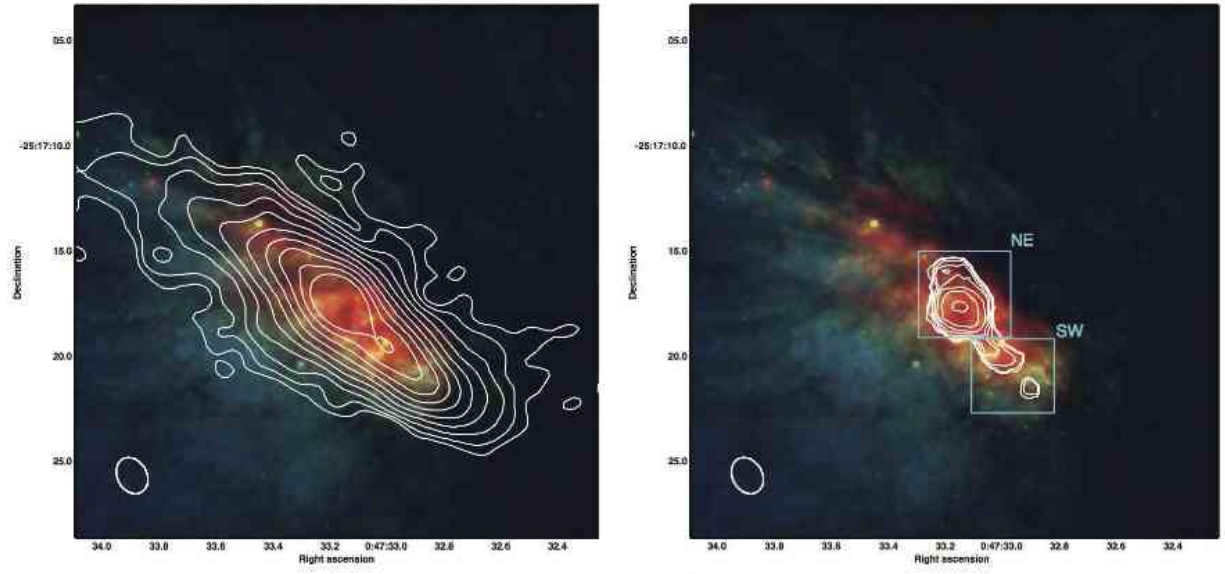


Fig. 19.— RRLs can measure the ionized gas properties in the dusty nuclei of starburst galaxies. The left panel shows JVL A observations of the 1cm continuum emission, which is mostly free-free emission, from the nuclear starburst of the edge-on galaxy NGC 253. The right panel shows JVL A observations of the H58 α emission from the same galaxy. The background image shows optical *HST* images. Paschen α is red, I band is green, and B band is blue. Figure from Kepley et al. (2011).

signpost for a specific phenomenon, a property which renders masers powerful astrophysical tools (Menten 2007). More precisely, masers are formed under specific conditions, and the detection of maser emission therefore suggests that physical conditions (e.g., temperature, density, and molecular abundance) in the region where the maser forms lie within a defined range (c.f., Cohen 1995, Ellingsen 2004, and references therein). Therefore, interferometric blind and targeted surveys of maser species can lead to the detection of objects at interesting evolutionary phases (Ellingsen 2007).

Table 6: ALMA bands with known maser lines (Menten 2007)

Species	ALMA Bands
H ₂ O	B3, B5, B6, B7, B8, B9
CH ₃ OH	B1, B3, B4, B6
SiO	B1, B2, B3, B4, B5, B6, B7
HCN	B3, B4, B6, B7, B9

Theoretical models of masers strongly depend on physical conditions as well as the geometry of the maser source. A successful model should be able to reproduce observational characteristics of observed maser lines but also to predict new maser transitions (e.g., the models of Sobolev 1997 for Class II methanol masers and Neufeld 1991 for water masers). In that respect, interferometry is essential for the successful search of candidate lines and confirmation of their maser nature. ALMA, in particular, will resolve closely spaced maser spots and help further establish precise models of masing sources by determining if the detected maser signals are associated with thermal emission (Sobolev 1999), which is essential for improving theoretical models. With Band 1, ALMA will cover an even wider frequency range, making it ideal for multi-transition observations of various maser species across the millimeter and submillimeter windows. Examples of species with observed maser radiation in the different ALMA bands are given in Table 6, while Tables 7 & 8 list SiO and methanol maser transitions that have been observed or predicted to be within Band 1.

Maser radiation can be linearly or circularly polarized depending on the magnetic properties of the molecule. Polarimetric studies of maser radiation with interferometers can therefore yield information on the morphology of the magnetic field threading the region on small scales, with the plane-of-sky and line-of-sight components of the field being probed using linear and circular polarization measurements, respectively (e.g., see Harvey-Smith 2008, Vlemmings 2006). Polarization data are essential for improving on the theory of maser polarization first introduced by Goldreich (1973a), which applies to a linear maser region, a

constant magnetic field, the simplest energy states for a masing transition, and asymptotic limits. Observations at higher spatial resolution are needed to verify and improve on more realistic and extensive models (Watson 2008).

In summary, the ALMA Band 1 frequency range contains numerous CH_3OH and SiO maser lines that can be observed to trace very distinct conditions in the ISM and probe maser production mechanisms. With ALMA’s high resolutions and sensitivities in the south, the Band 1 receivers will be able to trace easily masers from southern sources, and provide highly complementary data to masers observed in the higher frequency ALMA Bands.

Table 7: Observed SiO maser lines in the Band 1 of ALMA (Menten 2007).

Transitions	Frequency (GHz)
$v=0$ ($J=1 \rightarrow 0$)	42.373359
$v=3$ ($J=1 \rightarrow 0$)	42.519373
$v=2$ ($J=1 \rightarrow 0$)	42.820582
$v=0$ ($J=1 \rightarrow 0$)	42.879916
$v=1$ ($J=1 \rightarrow 0$)	43.122079
$v=0$ ($J=1 \rightarrow 0$)	43.423585

Table 8: Observed (Menten 2007) and predicted (designated with a star, Cragg et al. 2005) methanol maser lines in Band 1

Transitions	Frequency (GHz)
$4(-1) \rightarrow 3(0)\text{E}$	36.1693
$7(-2) \rightarrow 8(-1)\text{E}$	37.7037
$6(2) \rightarrow 5(3)\text{A}^+$	38.2933
$6(2) \rightarrow 5(3)\text{A}^-$	38.4527
$7(0) \rightarrow 6(1)\text{A}^+$	44.0694
$2(0) \rightarrow 3(1)\text{E}^*$	44.9558
$9(3) \rightarrow 10(2)\text{E}^*$	45.8436

6.2.5. Magnetic Field Strengths from Zeeman Measurements

Magnetic fields are believed to play a crucial role in the star formation process. Various theoretical and numerical studies explain how magnetic fields can account for the support of clouds against self-gravity, the formation of cloud cores, the persistence of supersonic line widths, and the low specific angular momentum of cloud cores and stars (McKee & Ostriker 2007). The standard model suggests that the initial mass-to-(magnetic) flux ratio, M/Φ_{init} , is the key parameter governing the fate of molecular cores. Namely, if the M/Φ_{init} of a core is greater than the critical value, the core will collapse and form stars on short time scales, but for cores with M/Φ_{init} smaller than the critical value the process of ambipolar diffusion will take a long time to reduce the magnetic pressure (Mouschovias & Spitzer 1976; Shu et al. 1987). On the other hand, recent MHD simulations suggest that turbulence can control the formation of clouds and cores. In such cases, the mass-to-flux ratio in the center of a collapsing core will be larger than that in its envelope, the opposite of the ambipolar diffusion results (Dib et al. 2007). Therefore, measuring the magnetic field strengths and the mass-to-flux ratios in the core and envelope provide a critical test for star formation theories.

Despite its central importance, the magnetic field is the most poorly measured parameter in the star formation process. The main problem is that magnetic fields can be measured only via polarized radiation, which requires extremely high sensitivity for detections. As a result, the observed data on magnetic fields is sparse compared with those related to the densities, temperatures, and kinematics in star-forming cores. The large collecting area of ALMA provides the best opportunity to resolve the sensitivity problem for magnetic field measurements.

The key to determining mass-to-flux ratios is the measurement of the strength of magnetic fields. This measurement can be made *directly* through detection of the Zeeman effect in spectral lines. Observations of Zeeman splitting involve detecting the small difference between left and right circular polarizations, which is generally very small in interstellar conditions (with the exception of masers). Successful non-maser detections of the Zeeman effect in molecular clouds have only been carried out with HI, OH, and CN lines because these species have the largest Zeeman splitting factors ($\sim 2 - 3.3 \text{ Hz}/\mu\text{G}$) among all molecular lines (Crutcher et al. 1996, 1999; Falgarone et al. 2008). Thermal HI and OH lines, however, probe relatively low-density gas ($n(\text{H}) < 10^4 \text{ cm}^{-3}$). Also, CN detections are difficult; Crutcher (2012) described only 8 CN Zeeman detections towards 14 positions observed with significant sensitivity.

ALMA Band 1 receivers provide the opportunity to detect the Zeeman effect from the CCS 4_3-3_2 line at 45.37903 GHz and hence greatly advance our understanding in star formation. CCS has been widely recognized as being present only very early in the star-

forming process through chemical models (Aikawa et al. 2001, 2005) and observations (Suzuki et al. 1992; Lai & Crutcher 2000). Therefore the mass-to-flux ratio derived from the CCS Zeeman measurements will be very close to the initial values before the onset of gravitational collapse. CCS 4_3-3_2 also has a relatively large Zeeman splitting factor (~ 0.6 Hz/ μ G; Shinnaga & Yamamoto 2000) compared to most molecules. ALMA’s antennas and site will be excellent at these “long” wavelengths, providing the stability and accuracy needed for such sensitive polarization work. The linearly polarized detectors on ALMA’s antennas will also be ideally suited to measurement of Stokes V signatures from CCS.

Using the BIMA survey results from Lai & Crutcher (2000), Figure 20 demonstrates that detections of CCS Zeeman effects can be achieved if the ALMA specifications for Band 1 receivers are met. Zeeman effect detection depends on two factors: the magnetic field strength and the line intensity. The two lines in Fig. 20 show the 3σ detection limits for Stokes V spectrum with channel width of 0.024 km s $^{-1}$ and 1 hr or 10 hr integration time for a range of magnetic field strengths and line intensities. The channel width is chosen to have at least 6 channels across the FWHM of the total intensity spectrum (Stokes I). If we scale the line intensity from Lai & Crutcher (2000) assuming the intensity distribution is uniform within the $30''$ BIMA beam, the expected line intensity would be around 0.1-0.4 Jy for ALMA observations with $10''$ beam. Therefore, Fig. 20 shows that for the magnetic fields of 0.2-1 mG (typical values estimated from the application of the Chandrasehkar-Fermi method to dust polarimetry in dense cores), we can detect the CCS Zeeman effect with reasonable on-source integration time (less than 10 hr).

Note that the SiO $v=1$, $J=1-0$ transition at 43.12 GHz could be also used to probe magnetic fields using the Zeeman effect, under certain circumstances. Though its Zeeman splitting factor is lower than that of the CCS 4_3-3_2 line, the Zeeman effect may be detectable in situations where the SiO line is extraordinarily bright, e.g., as a maser (see McIntosh, Predmore & Patel 1994). (Note, however, that non-Zeeman interpretations of circularly polarized SiO emission have also been advanced; see Weibe & Watson 1998).

In summary, ALMA Band 1 receivers will provide the opportunity to measure the initial mass-to-flux ratio of molecular cores through the detection of the Zeeman effect. ALMA’s linear feeds are ideally suited to measuring Stokes V and ALMA’s ability to recover extended, low surface brightness emission through the shorter baselines of the 12-m Array and the inclusion of the ACA will be critical. E.g., Roy et al. 2011 noted that the JVLA only recovered 1-13% of the integrated emission of CCS 2_1-1_0 observed in single-dish observations using the JVLA’s most compact (D) configuration.) The results from Zeeman splitting from ALMA will allow us to test realistically the expectations from theoretical and numerical models for the first time.

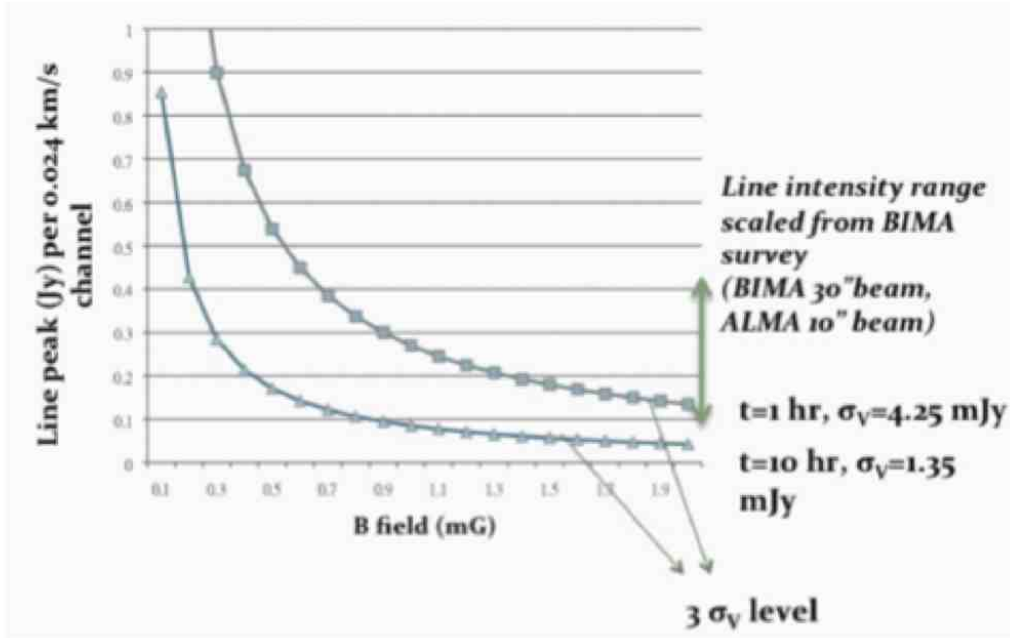


Fig. 20.— The expected detection limits (3σ) with integration time of 1 hr and 10 hr for a range of magnetic field strengths and CCS line intensity.

6.2.6. *Molecular Outflows from Young Stars*

The Submillimeter Array (SMA) has proven to be a successful instrument for the study of the youngest molecular outflows and jets from the most deeply embedded sources (e.g., Hirano et al. 2006; Palau et al. 2006; Lee et al. 2007a,b, 2008, 2009). The detection of excitation from rotational transitions of SiO up to levels $J=8-7$ and CO up to $J=3-2$ have uniquely identified a molecular high-velocity jet-like component located within outflow shells. This component displays similarities to the optical forbidden line jets observed in T-Tauri stars (Hirano et al. 2006; Palau et al. 2006; Codella et al. 2007; Cabrit et al. 2007). These observations have provided a new probe of how jets are launched and collimated during the earliest protostellar phase.

One unique opportunity offered by the Band 1 frequency range is observation of the $J=1-0$ transition of the SiO molecule at 43.424 GHz. This transition has not yet been detected nor surveyed around even the brightest molecular outflows, except using single-dish telescopes (Haschick & Ho 1990). One feature of this line that may be potentially distinct from the higher- J transitions of SiO is that it may be tracing the outer and more diffuse gas located on the outskirts of outflow shells that can be easily excited by shocks. Potential morphological and kinematic studies of the regions where the outflows interact with their own pre-natal clouds could be contrasted with other transitions using knowledge of their excitation conditions. In particular, the improved sensitivity to extended emission and higher image fidelity of ALMA make observations of SiO $J=1-0$ toward outflows more attractive with ALMA than with the JVL.

6.2.7. *Co-Evolution of Star Formation and Active Galactic Nuclei*

Roughly half of the high-redshift objects detected in CO line emission are believed to host an active galactic nucleus (AGN). Although they are selected based on their AGN properties, optically luminous high-redshift quasars exhibit many characteristics indicative of ongoing star formation, e.g., thermal emission from warm dust (Wang et al. 2008) or extended UV continuum emission. Indeed, galaxies with AGNs in the local Universe reveal a strong correlation between the mass (m) in their supermassive black hole (SMBH) and that of their stellar bulge (measured from the stellar velocity dispersion (σ); e.g., Kormendy & Richstone 1995; Magorrian et al. 1998; Gebhardt et al. 2000). Such a correlation can be explained if the SMBH formed coevally with the stellar bulge, implying that the luminous quasar activity signaling the formation of a sub-arcsecond SMBH at high-redshift should be accompanied by starburst activity. High spatial resolution observations of CO line emission in high-redshift quasars can be used to infer the dynamical masses, which are found to be

comparable to the derived molecular gas + black hole masses, meaning that their stellar component cannot contribute a large fraction of the total mass.

There is mounting evidence that quasar host galaxies at redshifts $z = 4\text{--}6$ have SMBH masses up to an order of magnitude larger than those expected from their bulge masses and the local relation (Walter et al. 2004; Riechers et al., in prep.), suggesting that the SMBH may have formed first. The possible time evolution of the $m - \sigma$ relation is of fundamental importance in studies of galaxy evolution, and this new finding needs to be made more statistically robust. Future observations of high-redshift AGN with the Band 1 receivers on ALMA would allow us to address this question through the study of low- J CO line emission in galaxies beyond redshifts $z \approx 1.3$ (see §4.2). ALMA especially allows studies of examples of such objects in the south that are not well observable (if at all) with the JVLBA.

6.2.8. *The Molecular Gas Content of Star-Forming Galaxies at $z \sim 2$*

While low- J CO line emission has only been detected in a few high-redshift objects, high- J CO line emission has been detected in more than sixty sources, most of which are classified as either submillimeter galaxies (SMGs) or far-infrared (FIR) luminous QSOs (see Carilli et al. 2011 for a review). Most of these studies have been conducted with sensitive interferometers and single-dish facilities operating in the 3 mm band (e.g., ALMA Band 3), which is sensitive to higher- J CO line transitions at high redshift, as is illustrated in Figure 6. These lines generally trace warmer and denser gas, and so previous data may have led to a bias in our understanding of the molecular gas properties of high-redshift galaxies (e.g., Papadopoulos & Ivison 2002). The addition of Band 1 receivers on ALMA will allow comparisons of the cold gas traced by the low- J transitions ($J=2\text{--}1/1\text{--}0$) in galaxies from moderate redshifts ($z \approx 1.3$) to those which existed when the Universe was re-ionized sometime before $z \gtrsim 6$.

Although many previous studies of CO line emission in high-redshift galaxies have focused on those starburst galaxies and AGN undergoing episodes of extreme star formation (e.g., $\gg 100 \text{ M}_\odot \text{ yr}^{-1}$), significant masses of molecular gas ($> 10^{10} \text{ M}_\odot$) have been discovered in more modest star-forming galaxies at $z = 1.5\text{--}2.0$ (Daddi et al. 2008). These “BzK” galaxies are selected for their location in a B- z -K colour diagram (Daddi et al. 2004) and have star-formation rates of $\sim 100 \text{ M}_\odot \text{ yr}^{-1}$ (Daddi et al. 2007), while their number density is roughly a factor of 30 larger than that of the more extreme SMGs at similar redshifts. Observations of CO $J=2\text{--}1$ line emission in these BzK galaxies reveal comparable masses of molecular gas to that of the SMGs, so their star-formation efficiencies appear lower. The excitation conditions of their molecular gas (temperature and density) are similar to those

of the Milky Way (Dannerbauer et al. 2008), as indicated by the “turnover” in the CO line spectral energy distribution occurring at the $J=3-2$ transition, i.e., lower than that of the SMGs which typically occurs at the $J=6-5$ or $J=5-4$ transition (Weiss et al. 2005). To develop a full spectral energy distribution for the CO line excitation, observations of these galaxies in the $J=1-0$ transition are needed with Band 1 receivers on ALMA. Such data will also provide a more robust estimate of the total molecular gas mass, along with the spatial resolution needed to constrain the gas kinematics, as has been done for the SMGs (Tacconi et al. 2006). Indeed, recent high-resolution studies of CO $J=1-0$ from lensed Lyman Break galaxies (Riechers et al. 2010) and unlensed BzK galaxies (Aravena et al., in prep.) have been made with the JVLA. Also, CO $J=1-0$ emission has been detected with the JVLA or GBT towards SMGs Ivison et al. 2010, 2011; Frayer et al. 2011; Riechers et al. 2011a,b). ALMA observations will allow similar important investigations to occur towards southern objects, especially those traced by ALMA itself in its higher-frequency Bands.

7. Summary

The Band 1 receiver suite has been considered an essential part of ALMA from the earliest planning days. Even through the re-baselining exercise in 2001, the importance of Band 1 was emphasized. With the ALMA Development Plan underway, we have undertaken an updated review of the scientific opportunity at these longer wavelengths. This document presents a set of compelling science cases over this frequency range. The science cases reflect the new proposed range of Band 1, 35-50 GHz (nominal) with an extension up to 52 GHz, which was in fact chosen to optimize the science return from Band 1. The science cases range from nearby stars and galaxies to the re-ionization edge of the Universe. Two provide additional leverage on the present ALMA Level One Science Goals and are seen as particularly powerful motivations for building the Band 1 receiver suite: (1) detailing the evolution of grains in protoplanetary disks, as a complement to the gas kinematics, requires continuum observations out to ~ 35 GHz (~ 9 mm); and (2) detecting CO 3 – 2 spectral line emission from Galaxies like the Milky Way during the era of re-ionization, $6 < z < 10$ also requires Band 1 receiver coverage. Band 1 receivers will also allow the pursuit of a diverse range of science cases that take advantage of the ALMA’s particular strengths over other facilities (e.g., the JVLA).

8. References

- Acke, B., & van den Ancker, M. E. 2004, *A&A*, 426, 151
- Acke, B., et al. 2004, *A&A*, 422, 621
- Adams, F. C., Emerson, J. P., & Fuller, G. A. 1990, *ApJ*, 357, 606
- Anglada, G. 1995, *RMAACS*, 1, 67
- Aikawa, Y., Ohashi, N., Inutsuka, S.-I., Herbst, E., & Takakuwa, S. 2001, *ApJ*, 552, 639
- Aikawa, Y., Herbst, E., Roberts, H., & Caselli, P. 2005, *ApJ*, 620, 330
- Andrews, S., & Williams, J. P. 2007a, *ApJ*, 659, 705
- Andrews, S., & Williams, J. P. 2007b, *ApJ*, 671, 1800
- Aschwanden, M. J., Wills, M. J.; Hudson, H. S., Kosugi, T., Schwartz, R. A. 1996, *ApJ*, 468, 398
- Bailey, J., Chrysostomou, A., Hough, J. H., Gledhill, T. M., McCall, A., Clark, S., Menard, F., & Tamura, M. 1998, *Science*, 281, 672
- Bartel, N. et al. 2002, *ApJ*, 581, 404
- Bartel, N., Bietenholz, M.F., Rupen, M.P., & Dwarkadas, V.V. 2007, *ApJ*, 668, 924
- Bauer, F. E., et al. 2008, *ApJ*, 688, 1210
- Beckwith, S., Sargent, A. I., Chini, R. S., & Guesten, R. 1990, *AJ*, 99, 924
- Beckwith, S., & Sargent, A. I. 1991, *ApJ*, 381, 250
- Bertoldi, F. et al. 2003, *A&A*, 409, L47
- Bietenholz, M. F., Bartel, N., & Rupen, M. P. 2004, *Science*, 304, 1947
- Bietenholz, M. F., Bartel, N., & Rupen, M. P. 2010, *ApJ*, 712, 1057
- Blain, A. W., Smail, I., Ivison, R. J., Kneib, J.-P., & Frayer, D. T. 2002, *Phys. Rep.*, 369, 111
- Boley, A., et al. 2012, *ApJ*, 750, L21
- Bonamente, M., Joy, M., LaRoque, S. J., et al. 2008, *ApJ*, 675, 106
- Birkinshaw, M. 1999, *Phys. Rep.* 310, 97

- Buckle, J. V., et al. 2006, *Faraday Discussions*, 133, 63
- Bouwens, R. J., et al. 2009, *ApJ*, 690, 1764
- Boss, A. 2005, *ApJ*, 629, 535
- Butler, B., 2010, VLA Test Memo 232, “Atmospheric Opacity at the VLA”
- Butler, B., 1998, VLA Memo 237, “Precipitable Water at the VLA – 1990-1998”
- Butler, B. & Desai, K., VLA Test Memo 222, “Phase Fluctuations at the VLA Derived From One Year of Site Testing Interferometer Data”
- Cabrit, S., et al. 2007, *A&A*, 468, L29
- Calvet, N., et al. 2002, *ApJ*, 568, 1008
- Cappelluti, N., Predehl, P., Böhringer, H., et al. 2011, *Memorie della Societa Astronomica Italiana Supplementi*, 17, 159
- Carilli, C. L., et al. 2007, *ApJ*, 666, L9
- Carilli, C. L., et al. 2008, *Ap&SS*, 313, 307
- Carlstrom, J. E., Holder, G. P., & Reese, E. D. 2002, *ARA&A*, 40, 643
- Casassus, S., et al. 2008, *MNRAS*, 391, 1075
- Chevalier, R.A. 1982, *ApJ*, 259, 85
- Churchwell, E. 2001, *ARA&A*, 40, 27
- Cohen, R. J. 1995, *Ap&SS*, 224, 55
- Codella, C., et al. 2007, *A&A*, 462, L53
- Cool, R.J., et al. 2006, *AJ*, 132, 823
- Cragg, D. M., Sobolev, A. M., & Godfrey, P. D. 2005, *MNRAS*, 360, 533
- Crutcher, R. M. 2012, *ARA&A*, 50, 29
- Crutcher, R. M., Troland, T. H., Lazareff, B., & Kazes, I. 1996, *ApJ*, 456, 217
- Crutcher, R. M., Troland, T. H., Lazareff, B., Paubert, G., & Kazès, I. 1999, *ApJL*, 514, 121
- D’Addario, L., & Holdaway, M. 2003, ALMA Memo 521, “Joint Distribution of Atmospheric Transparency and Phase Fluctuations at Chatnantor”
- Daddi, E., et al. 2004, *ApJ*, 617, 746

- Daddi, E., et al. 2007, ApJ, 670, 156
- Daddi, E., et al. 2008, ApJL, 673, L21
- Dannerbauer, H., et al. 2009, ApJL, 698, 178
- Dark Energy Survey Collaboration, The 2005, arXiv:astro-ph/0510346
- Dib, S., Kim, J., Vázquez-Semadeni, E., Burkert, A., & Shadmehri, M. 2007, ApJ, 661, 262
- Dodds-Eden, K., et al. 2009, ApJ, 698, 676
- Draine, B. 2003, ARA&A, 41, 241
- Draine, B. 2006, ApJ, 636, 1114
- Draine, B., & Anderson, N. 1985, ApJ, 292, 494
- Draine, B., & Lazarian, A. 1998, ApJ, 508, 157
- Dullemond, C. P., & Dominik, C. 2005, A&A, 434, 971
- Dunkley, J., et al. 2009, ApJS, 180, 306
- Dunkley, J., Hlozek, R., Sievers, J., et al. 2011, ApJ, 739, 52
- Eckart, A., et al. 2006, *A*, 450, 535
- Ellingsen, S. P. et al. 2007, IAUS, 242, 213
- Ellingsen, S. P. 2004, IAUS, 221, 133
- Ettori, S., & Fabian, A. C. 2006, MNRAS, 369, L42
- Falgarone, E., Troland, T. H., Crutcher, R. M., & Paubert, G. 2008, A&A, 487, 247
- Fan, X., et al. 2001, AJ, 122, 2833
- Fan, X., et al. 2006a, AJ, 132, 117
- Fan, X., Carilli, C. L., & Keating, B. 2006b, ARA&A, 44, 415
- Fender, R. P., et al. 1999, ApJL, 519, 165
- Finkbeiner, D. P., Schlegel, D. J., Frank, C., & Heiles, C. 2002, ApJ, 566, 898
- Freyer, D., et al. 2011, ApJ, 726, L22
- Gaensler, B. M., et al. 2007, AIP Confer. Ser., ed. S. Immler & R. McCray, 937, 86
- Garrod, R. T., Weaver, S. L. W., & Herbst, E. 2008, ApJ, 682, 283

- Gebhardt, K., et al. 2000, ApJ, 543, L5
- Geisbuesch, J., & Hobson, M. P. 2007, MNRAS, 382, 158
- Geisbuesch, J., Kneissl, R., & Hobson, M. P. 2005, MNRAS, 360, 41
- Ghez, A., et al. 2008, ApJ, 689, 1044
- Gillessen, S., et al. 2009, ApJ, 692, 1075
- Glikman, E., et al. 2008, AJ, 136, 954
- Goldreich, P., Keeley, D. A., & Kwan, J. Y. 1973, ApJ, 179, 111
- Greaves, J., Richards, A. M. S., Rice, W. K. M., & Muxlow, T. W. B. 2008, MNRAS, 391, 74
- Guilloteau, S., et al. 2009, *a*, 529, 105
- Gunn, J.E., & Peterson, B.A. 1965, ApJ, 142, 16331
- Hales, A. S., et al. 2004, ApJ, 613, 977
- Haschick, A. D., & Ho, P. T. P. 1990, ApJ, 352
- Harvey-Smith, L., Soria-Ruiz, R., Duarte-Cabral, A., & Cohen, R. J. 2008, MNRAS, 384, 719
- Helfand, D. J., Gotthelf, E. V., & Halpern, J. P. 2001, ApJ, 556, 380
- Hincks, A. D., et al. 2009, arXiv:0907.0461
- Hirano, N., et al. 2006, ApJL, 636, 141
- Holtom, P. D., Bennett, C. J., Osamura, Y., Mason, N. J., & Kaiser, R. I. 2005, ApJ, 626, 940
- Hu, E.,M., Cowie, L. L., & McMahon, R. G. 1998, ApJ, 502, L99
- Hunt-Cunningham, M. R., & Jones, P. A. 2004, IAUS, 213, 159
- Isella, A, Natta, A., Wilner, D., Carpenter, J. M., & Testi, L. 2010, ApJ, 725, 1735
- Ivison, R. J., et al. 2010, MNRAS, 404, 198
- Ivison, R. J., et al. 2011, MNRAS, 412, 1913
- Iye, M., et al. 2006, Nature, 443, 186
- Kaufmann, P., Raulin, J.-P., de Castro, C. G. G. 2004, ApJ, 603, L121

- Kepley, A. A., Chomiuk, L., Johnson, K. E., Goss, W. M., Balser, D. S., & Pisano, D. J. 2011, *ApJ*, 739, L24
- Kitayama, T., Komatsu, E., Ota, N., Kuwabara, T., Suto, Y., Yoshikawa, K., Hattori, M., & Matsuo, H. 2004, *PASJ*, 56, 17
- Koerding E. G., Fender R. P., & Migliari S. 2006, *MNRAS*, 369, 1451
- Komatsu, E., Matsuo, H., Kitayama, T., Kawabe, R., Kuno, N., Schindler, S., & Yoshikawa, K. 2001, *PASJ*, 53, 57
- Kormendy, J., & Richstone, D. 1995, *ARA&A*, 33, 581
- Korngut, P. M., Dicker, S. R., Reese, E. D., et al. 2011, *ApJ*, 734, 10
- Lai, S.-P., & Crutcher, R.M. 2000, *ApJS*, 128, 271
- Lakićević, M., Zarnado, G., van Loon, Th., Staveley-Smith, L., Potter, T., Ng, C.-Y., & Gaensler, B. M. 2012, *A&A*, 541, L2
- Lee, C.-F., et al. 2007a, *ApJ*, 659, 499
- Lee, C.-F., et al. 2007b, *ApJ*, 670, 1188
- Lee, C.-F., et al. 2008, *ApJ*, 685, 1026
- Lee, C.-F., et al. 2009, *ApJ*, 699, 1584
- Lee, J., & Komatsu, E. 2010, *ApJ*, 718, 60
- Leger, A., & Puget, J. L. 1984, *A&A*, 137, L5
- Li, Y., et al. 2007, *ApJ*, 665, 187
- Li, Y., et al. 2008, *ApJ*, 678, 41
- Lim, J., & Takakuwa, S. 2006, *ApJ*, 653, 425
- Lonsdale, C. J., et al. 2006, *ApJ*, 647, 185
- Maccarone T. J., 2008, *ASPC*, 401, 191
- Maccarone T. J., Gallo E., Fender R. P. 2003, *MNRAS*, 345, L19
- Magorrian, J., et al. 1998, *AJ*, 115, 2285
- Maness, H. et al. 2008, *ApJ*, 686, L25
- Mannings, V., & Emerson, J. 1994, *MNRAS*, 267, 361

- Markevitch, M., et al. 2000, ApJ, 541, 542
- Markevitch, M., et al. 2002, ApJ, 567, L27
- Markevitch, M., et al. 2009, arXiv:0902.3709
- Mason, B. S., Dicker, S. R., Korngut, P. M., et al. 2010, ApJ, 716, 739
- Masuda, S., Kosugi, T., Hara, H., Tsuneta, S., Ogawara, Y. 1994, Nature, 371, 495
- McIntosh, G. C., Read Predmore, C., & Patel, N. A. 1994, ApJ, 428, L29
- McKee, C. F. & Ostriker, E. C. 2007, ARA&A, 45, 565
- Melis, C., et al. 2011, ApJ, 739, L7
- Menanteau, F., Hughes, J. P., Sifon, C., et al. 2011, arXiv:1109.0953
- Menten, K. 2007, IAUS, 242
- Merloni, A., et al. 2012, arXiv, 1209.3114
- Migliari S., Fender R. P., Rupen, M., Wachter, S., Jonker, P. G., Homan, J., & van der Klis, M. 2004, MNRAS, 351, 186
- Morandi, A., Ettori, S., & Moscardini, L. 2007, MNRAS, 379, 518
- Mortlock, D. J., et al. 2008, arXiv0810.4180
- Mouschovias, T.Ch. & Spitzer, L., Jr. 1976, ApJ, 210, 326
- Narayanan, D., et al. 2008, ApJS, 174, 13
- Narayan, R., Ozel, F., & Sironi, L. 2012, ApJ, 757, L20
- Narayan R., & Yi, I. 1994, ApJL, 428, 13
- Neufeld, D., & Melnick, G. 1991, ApJ, 368, 215
- Ota, K., et al. 2008, ApJ, 677, 12
- Otárola, A., Holdaway, M., Nyman, L-Å, Radford, S. J. E., & Butler, B. J. 2005, ALMA Memo 512, “Atmospheric Transparency at Chajnantor: 1973-2003”
- Palau, A., et al. 2006, ApJL, 636, 137
- Papadopoulos, P. P. & Ivison, R. J. 2002, ApJ, 564, L9
- Pascucci, I., Gorti, U., & Hollenbach, D. 2012, ApJ, 751, L42

- Peters, T., Longmore, S. N., & Dullemond, C. P. 2012, MNRAS, 425, 2352
- Pfrommer, C., Enßlin, T. A., & Sarazin, C. L. 2005, A&A, 430, 799
- Plagge, T., et al. 2012, arXiv:1203.2175
- Planck Collaboration, Ade, P. A. R., Aghanim, N., et al. 2011, arXiv:1101.2024
- Pinte, C., Menard, F., Duchêne, G., & Bastien, P. 2006, A&A, 459, 797
- Pinte, C., et al. 2009, A&A, 498, 967
- Pollack, J., et al. 1996, Icarus, 124, 62
- Poole, G. B., Babul, A., McCarthy, I. G., et al. 2007, MNRAS, 380, 437
- Rafikov, R. 2006, ApJ, 646, 288
- Reid, M. J. & Brunthaler, A. 2004, ApJ, 616, 872
- Reipurth, B., & Bally, J. 2001, ARA&A, 39, 403
- Rephaeli, Y. 1995, ARA&A, 33, 541
- Rhoads J. E., et al. 2000, ApJ, 545, L85
- Ricci, L., Testi, L., Natta, A., Neri, R., Cabrit, S., & Herczeg, G. 2010, *a*, 512, 15
- Riechers, D., et al. 2009, ApJ, 703, 1338
- Riechers, D., et al. 2010, ApJ, 724, L153
- Riechers, D., et al. 2011a, ApJ, 733, L11
- Riechers, D., et al. 2011b, ApJ, 739, L31
- Rodmann, J., et al. 2006, A&A, 446, 211
- Rodríguez, L. F., et al. 1998, Nature, 395, 355
- Rodríguez, L. F., et al. 2003, ApJL, 586, 137
- Roy, N., Datta, A., Momjian, E. & Sarma, A. P. 2011, ApJ, 739, L4
- Sarazin, C.L. 1988, in “X-ray emission from clusters of galaxies,” Cambridge University Press
- Scaife, A. M. M., et al. 2009, MNRAS, 400, 1394
- Scaife, A. M. M., et al. 2010, MNRAS, 403, 46
- Sehgal, N., Trac, H., Acquaviva, V., et al. 2011, ApJ, 732, 44

- Shang, H., Lizano, S., Glassgold, A., & Shu, F. 2004, *ApJL*, 612, 69
- Sheperd, D. S., Chandler, C. J., Cotton, B., Perley, R. A., Randall, S. K., & Remijan, A. J. 2013, *High Energy Density Physics*, 9, 26
- Shinnaga, H., & Yamamoto, S. 2000, *ApJ*, 544, 330
- Shu, F. H., Adams, F. C., & Lizano, S. 1987, *ARA&A*, 25, 23
- Sobolev, A. M., et al. 1999, in *The Physics and Chemistry of the Interstellar Medium*, ed. V. Ossenkopf et al. (GCA-Verlag: Herdecke), 299
- Sobolev, A. M., Cragg, D. M., Godfrey, P. D. 1997, *MNRAS*, 288, L39
- Staniszewski, Z., et al. 2009, *ApJ*, 701, 32
- Sui, L., Holman, G. D. 2003, *ApJ*, 596, L251
- Sunyaev, R. A., & Zel'dovich, Ya. B. 1972, *Comm. Astrophys. Space Phys.* 4, 173
- Sutton, E. C., et al. 2001, *ApJ*, 554, 173
- Suzuki, H., et al. 1992, *ApJ*, 392, 551
- Tacconi L. J., et al. 2006, *ApJ*, 640, 228
- Takakuwa, S., Kamazaki, T., Saito, M., & Hirano, N. 2003, *ApJ*, 584, 818
- Tananbaum H., Gursky H., Kellogg E., Giacconi R., & Jones C. 1972, *ApJ*, 177, L5
- Taniguchi, Y., et al. 2005, *PASJ*, 57, 165
- Testi, L., Natta, A., Shepherd, D.S., & Wilner, D.J. 2001, *ApJ*, 554, 1087
- Tudose, V., Fender, R. P., Linares, M., Maitra, D., & van der Klis M. 2009, *MNRAS*, 400, 2111
- Vikhlinin, A., Kravtsov, A. V., Burenin, R. A., et al. 2009, *ApJ*, 692, 1060
- Vlemmings, W. H. T., Diamond, P. J., & Imai, H. 2006, *IAUS*, 234, 267
- Wagg, J., & Kanekar, N. 2012, *ApJ*, 751, L24
- Wagg, J., Kanekar, N., & Carilli, C.L. 2009, *ApJL*, 697, L33
- Walter, F., et al. 2003, *Nature*, 424, 406
- Walter, F., et al. 2004, *ApJ*, 615, L17
- Walter, F., et al. 2009, *ApJ*, 691, L1

- Wang, R., et al. 2008, *AJ*, 135, 1201
- Wang, R., et al. 2010, *ApJ*, 714, 699
- Wang, R., et al. 2011a, *AJ*, 142, 101
- Wang, R., et al. 2011b, *ApJ*, 739, L34
- Watson, W. D. 2008, arXiv0811.1292W
- Weintraub, D. A., Sandell, G., & Duncan, W. D. 1989, *ApJ*, 340, 69
- Weiss, A., Downes, D., Walter, F., & Henkel, C. 2005, *A&A*, 440, 45
- Welch, W. J., et al. 2004, in *Bioastronomy 2002*, eds R. Norris, F. Stootman (ASP, San Francisco), 213, 59
- Weiler, K. W., Panagia, N., Montes, M. J., & Sramek, R. A. 2002, *ARA&A*, 40, 387
- Weibe, D. S., & Watson, W. D. 1998, *ApJ*, 503, L71
- White, S. M., Krucker, S., Shibasaki, K., et al. 2003, *ApJ*, 595, L111
- Wik, D. R., Sarazin, C. L., Ricker, P. M., & Randall, S. W. 2008, *ApJ*, 680, 17
- Williamson, R., Benson, B. A., High, F. W., et al. 2011, *ApJ*, 738, 139
- Willott, C. J., et al. 2009, *AJ*, 137, 3541
- Wilner, D. J., Ho, P. T. P., Kastner, J. H., & Rodriguez, L. F. 2000, *ApJ*, 534, 101
- Wootten, A. 2007, *IAUS*, 242
- Wyatt, M. C., 2009, *ARA&A*, 46, 339
- Yamada, K., et al. 2012, *PASJ*, in press.
- Yokoyama, T., Akita, K., Morimoto, T., Inoue, K., Newmark, J. 2001, *ApJ*, 546, L69
- Yusef-Zadeh, F., et al. 2012, *ApJ*, 757, L1
- Yusef-Zadeh, F., et al. 2006, *ApJ*, 650, 189